Energy & Environmental Science

PAPER

View Article Online
View Journal

Published on 11 February 2016. Downloaded by University of California - Irvine on 11/02/2016 18:07:40.

Cite this: DOI: 10.1039/c6ee00129g

Textured nanoporous Mo:$BiVO_4$ photoanodes with high charge transport and charge transfer quantum efficiencies for oxygen evolution†

Vineet Nair,[a] Craig L. Perkins,[b] Qiyin Lin[c] and Matt Law*[acd]

Received 14th January 2016,
Accepted 3rd February 2016

DOI: 10.1039/c6ee00129g

www.rsc.org/ees

We have developed a simple spin coating method to make high-quality nanoporous photoelectrodes of monoclinic $BiVO_4$ and studied the ability of these electrodes to transport photogenerated carriers to oxidize sulfite and water. Samples containing molybdenum and featuring [001] out-of-plane crystallographic texture show a photocurrent and external quantum efficiency (EQE) for sulfite oxidation as high as 3.1 mA cm^{-2} and 60%, respectively, at 1.23 V *versus* reversible hydrogen electrode. By using an optical model of the electrode stack to accurately determine the fraction of electrode absorptance due to the $BiVO_4$ active layer, we estimate that on average 70 ± 5% of all photogenerated carriers escape recombination. A comparison of internal quantum efficiency as a function of film processing, illumination direction, and film thickness shows that electron transport is efficient and hole transport limits the photocurrent (hole diffusion length <40 nm). We find that Mo addition primarily improves electron transport and texturing mostly improves hole transport. Mo enhances electron transport by thinning the surface depletion layer or passivating traps and recombination centers at grain boundaries and interfaces, while improved hole transport in textured films may result from more efficient lateral hole extraction due to the texturing itself or the reduced density of deep gap states observed in photoemission measurements. Photoemission data also reveal that the films have bismuth-rich, vanadium- and oxygen-deficient surface layers, while ion scattering spectroscopy indicates a Bi–V–O surface termination. Without added catalysts, the plain $BiVO_4$ electrodes oxidized water with an initial photocurrent and peak EQE of 1.7 mA cm^{-2} and 30%, respectively, which equates to a hole transfer efficiency to water of >64% at 1.23 V. The electrodes quickly photocorrode during water oxidation but show good stability during sulfite oxidation and indefinite stability in the dark. By improving the hole transport efficiency and coating these nanoporous $BiVO_4$ films with an appropriate protective layer and oxygen evolution catalyst, it should be possible to achieve highly efficient and stable water oxidation at a practical pH.

Introduction

The ability to perform photoelectrolysis of water using efficient, stable, and earth abundant materials may be essential for making renewable hydrogen a replacement for fossil fuels. Since its discovery as a photocatalyst in 1998,[1] n-type monoclinic bismuth vanadate (m-$BiVO_4$, or BVO) has gained increasing interest as a model metal oxide photoanode for O_2 evolution,[2–5] owing to its (indirect) band gap of 2.4–2.5 eV (496–517 nm), optical absorption coefficient of 10^4–10^5 cm^{-1} for $h\nu$ = 2.5–3.5 eV,[6,7] flat band potential <200 mV positive of the hydrogen evolution reaction (HER), which enables oxygen evolution at a lower bias than many other metal oxides,[8] and a reported photocurrent density for the oxygen evolution reaction (OER) as high as 4.5–5 mA cm^{-2} at the OER potential (+1.23 V *versus* reversible hydrogen electrode) for single-component BVO electrodes under simulated 1 sun (100 mW cm^{-2}) AM1.5G illumination.[9,10] Based on its relatively large band gap, BVO has a maximum theoretical photocurrent of 6.2–7.5 mA cm^{-2} and solar-to-hydrogen conversion efficiency of 7.6–9.2% when paired with an ideal photocathode in a tandem water-splitting device. Reducing the band gap of BVO to 1.8–2.2 eV *via* alloying, doping, strain, or other types of band gap engineering is thus an important goal for making practical water splitting devices based on this material.[10–13] Although its non-optimal band gap restricts its ultimate efficiency, poor charge transport is the more immediate limitation on the photoelectrochemical performance of BVO. BVO is reported to

[a] Department of Chemical Engineering and Materials Science, University of California, Irvine, Irvine, CA 92697, USA. E-mail: matt.law@uci.edu
[b] National Renewable Energy Laboratory, Golden, CO 80401, USA
[c] Laboratory for Electron and X-ray Instrumentation, University of California, Irvine, Irvine, CA 92697, USA
[d] Department of Chemistry, University of California, Irvine, Irvine, CA 92697, USA

† Electronic supplementary information (ESI) available. See DOI: 10.1039/c6ee00129g

Published on 11 February 2016. Downloaded by University of California - Irvine on 11/02/2016 18:07:40.

have relatively short diffusion lengths both for holes[14–17] (which motivates the design of nanostructured films to achieve efficient hole collection) and electrons[18–20] (which forces the use of optically thin films for efficient electron collection). Other key shortcomings of BVO include its poor activity for the OER in the absence of a catalyst[14,21] and low intrinsic stability, especially under the acidic or basic conditions (pH < 3 or pH > 11)[22] that are desirable to avoid ion gradients and mass transport limitations in practical solar fuel generators.[23]

Most research on BVO has focused on improving the photoelectrochemical performance of BVO thin films by employing some combination of nanostructuring to improve hole collection,[9,10,18,24,25] "doping" (particularly with W and Mo) to improve electron transport,[10,14,15,18,21,24,26–43] heterostructures (*e.g.*, WO_3/BVO and SnO_2/BVO) to improve charge separation and device fill factor,[19,25,30,32,35,36,37,44–50] and catalyst layers (*e.g.*, cobalt phosphate, CoO_x, metal oxyhydroxides)[8,9,14,18,20–22,25,30,37,39,50–56] to promote water oxidation and enhance BVO stability. Comparatively little work has been done to understand and optimize the light absorption, charge transport, and charge transfer properties of BVO itself.

Here, we investigate the ability of high-quality, single-component BVO films (no buried junctions or surface coatings) to deliver photogenerated carriers for the oxidization of sulfite and water. We use a simple spin-coating method to make nanoporous BVO films with and without molybdenum impurities and preferred crystallographic orientation (texturing). The Mo-containing, textured films show the best performance, with a charge transport quantum efficiency of 70 ± 5%, an initial hole transfer quantum efficiency for water oxidation greater than 60%, and photocurrents for sulfite and water oxidation as high as 3.1 mA cm^{-2} and 1.7 mA cm^{-2}, respectively, under standard 1 sun illumination at the OER potential. By comparing the photocurrent and external quantum efficiency of the four types of BVO films as a function of illumination direction in sulfite electrolyte, we show that Mo mostly improves electron transport while texturing mostly improves hole transport. Likely mechanisms for the action of Mo are described. Photoemission measurements reveal that the textured films have a much lower concentration of a previously unreported defect state deep within the BVO band gap, which can explain the better hole transport in the textured films. A simple model shows that the hole diffusion length of the Mo-containing, textured films is at most 40 nm. Absorptance and internal quantum efficiency data acquired with the aid of an optical model and as a function of BVO thickness and illumination direction reveal that electron transport is highly efficient and the photocurrent of the best films is limited by hole transport. We use photoelectron spectroscopy and ion scattering spectroscopy to show that the films have a bismuth-rich, vanadium- and oxygen-deficient surface layer with a Bi–V–O surface termination. The electrodes are found to photocorrode rapidly during water oxidation *via* bulk dissolution of the BVO film, whereas stability is much better in sulfite, suggesting that BVO can be stabilized by appropriate surface protection layers and catalysts. Increasing the hole transport efficiency of our plain BVO films from ~70% to ~100% might be achieved in several ways, including more complete passivation of the deep gap states to further increase the hole diffusion length, better nanostructuring of the films to eliminate grain boundaries and shorten the hole transit distance, and tuning the composition of the surface layer to promote the drift of holes to the BVO surface. A combination of these strategies should boost the performance of BVO photoanodes close to theoretical limits.

Results and discussion

Synthesis and physical characterization of the BVO films

We prepared four different types of porous, nanostructured thin films of phase-pure monoclinic $BiVO_4$ (BVO) by spin coating an ethylene glycol solution containing $Bi(NO_3)_3$ and $VO(acac)_2$ plus the triblock copolymer Pluronic F-108 onto glass substrates coated with fluorine-doped tin oxide (FTO) and annealing the resulting films at 475 °C in air for 15 minutes (see Experimental section and Schemes S1–S3 in the ESI†). Solutions containing equimolar amounts of $Bi(NO_3)_3$ and $VO(acac)_2$ but no molybdenum (Mo) produced highly porous and crystalline films of monoclinic $BiVO_4$ with powder-like (crystallographically untextured) X-ray diffraction patterns (Fig. 1a and e). We refer to these Mo-free, crystallographically untextured samples as "noMo/U" films. We discovered that solutions with twice the amount of $VO(acac)_2$ yield BVO films with pronounced *c*-axis texture normal to the substrate plane (Fig. 1b and e and Fig. S1 (ESI†). Note that we use the unit cell of the $I2/b$ space group of m-BVO throughout this paper, including when discussing previous work) and improved photoanode performance (*vide infra*). Such Mo-free, textured samples are designated "noMo/T" films. To assess the impact of incorporating molybdenum, an impurity known to improve the photocurrent of $BiVO_4$ electrodes,[18,21,26,30,31,33,34,37,40,42] we added Mo to untextured and textured BVO films (making "Mo/U" and "Mo/T" films, respectively) by spiking the spin coating solution with 2 at% $MoO_2(acac)_2$ (see Experimental and Fig. 1c–e). As shown below, the performance of the Mo/T photoanodes is particularly good, and, since the Mo/T films were found to perform best when ~220 nm thick, we focus mostly on ~220 nm thick films in this study.

Plan view and cross-sectional scanning electron microscopy (SEM) images of noMo/U, noMo/T, Mo/U, and Mo/T films of approximately the same thickness (220 ± 10 nm) are shown in Fig. 1a–d. Each film resembles a mat of partially fused rod-shaped bacteria. The noMo/U films have the smallest average rod diameter (~45 nm), whereas the particles are thicker (65–70 nm) and more fused in three other types of films. The textured films are less porous than the untextured films, which is the main reason for the larger optical absorbance of textured samples at wavelengths larger than ~325 nm (Fig. 1h). The particles of the textured films also have rougher, more jagged shapes as a result of the brief KOH etch that is used to remove V_xO_y phase impurities from these films. Other than their lower porosity and more jagged particle shapes, the textured films have a very similar morphology to the Mo/U films. All of the films are phase-pure monoclinic $BiVO_4$ by XRD (Fig. 1e) and

 This journal is © The Royal Society of Chemistry 2016

Published on 11 February 2016. Downloaded by University of California - Irvine on 11/02/2016 18:07:40.

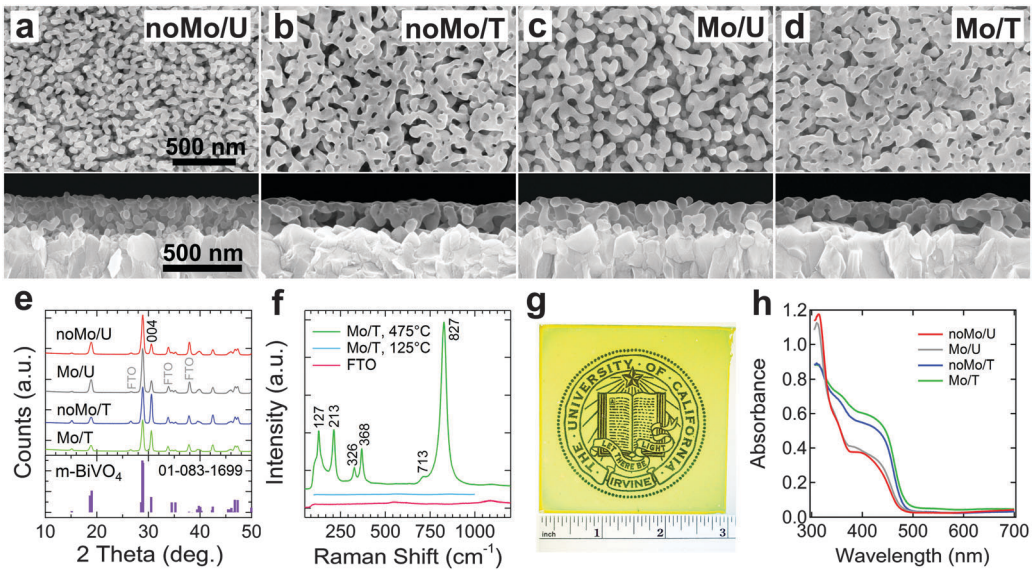

Fig. 1 Structural and optical characterization of nanostructured $BiVO_4$ electrodes. Plan view and cross section SEM images of $BiVO_4$ films on FTO-coated glass substrates made (a) with no Mo and untextured (noMo/U), (b) with no Mo and textured (noMo/T), (c) with 2% Mo and untextured (Mo/U), and (d) with 2% Mo and textured (Mo/T). All BVO films are ~220 nm thick and imaged at the same magnification. (e) Grazing incidence XRD patterns of the films. All peaks other than those from the FTO substrate correspond to monoclinic $BiVO_4$ (PDF # 01-083-1699, *I*2/*b* space group; reference lines shown at bottom). (f) Raman spectrum of a typical Mo/T film annealed at 475 °C, showing the characteristic peaks of monoclinic BVO.[57] A Mo/T film annealed at only 125 °C and a bare FTO-coated glass substrate are shown for comparison. The film is crystalline only after high-temperature annealing. The major Raman peak at 827 cm^{-1} (assigned to the symmetric stretching mode of VO_4^{3-} units) shows a very small shift to lower energy with increasing Mo concentration in the ink (Fig. S3, ESI†). (g) Photograph of a 3 × 3 inch Mo/T film prepared on FTO-coated glass. (h) Absorbance spectra of the four BVO films on FTO-coated glass substrates measured with an integrating sphere. Absorbance = $-\log(T + R)$, where T is transmittance and R reflectance. Light is incident from the BVO side. Optical modeling of the thin-film stacks (see Experimental) show that the higher porosity of the untextured films results in lower reflectance and larger absorbance than the textured films for wavelengths <325 nm. See Fig. S4 (ESI†) for Tauc fits of the indirect and direct band gap of each film.

Raman spectroscopy (Fig. 1f), with no trace of other phases detected even in synchrotron XRD experiments (data not shown). Films made from solutions containing up to 3 at% Mo were also phase pure by XRD (Fig. S2, ESI†), but a $Bi_4V_2O_{11}$ impurity appeared in films made with 4 at% or more $MoO_2(acac)_2$. Relative to the untextured films, the textured films have ~3 times larger 004 and 002 XRD peaks, ~2 times smaller 101 and 011 peaks, and ~1.5 times smaller 020 and 200 peaks (at 2θ = 30.53, 15.13, 18.67, 18.99, 34.51 and 35.24 degrees, respectively), indicating significant [001] preferred orientation in the textured films (Fig. 1). A more detailed analysis of film texture was carried out using complementary powder XRD and pole figure measurements, described below (see Fig. 5).

The nature of charge transport in a polycrystalline photoelectrode can depend considerably on the size of the crystallites and the number of grain boundaries along the transport path. This is because grain boundaries often feature energy barriers and high rates of trapping and recombination that degrade carrier mobility and lifetime. We used Scherrer line broadening analysis of $\theta/2\theta$ XRD patterns to estimate the size of the BVO crystallites normal to the plane of the films (see Experimental). Using the 004 reflection, we find an average crystallite diameter of 35 ± 5 nm for noMo/U films, 47 ± 5 nm for Mo/U films, 59 ± 5 nm for noMo/T films, and 60 ± 5 nm for Mo/T films. Averaging data from the six most prominent reflections gives an effective crystallite size of 34 ± 4 nm, 43 ± 4 nm, 47 ± 8 nm, and 48 ± 7 nm for the four films (Table 1). The crystallites in each film are thus slightly smaller than the shortest particle dimension measured in SEM images, meaning that holes probably encounter zero or at most a few grain boundaries before reaching the BVO surface. However, since the crystallites are 4–6 times smaller than the film thickness, electrons must transit a significant number of grain boundaries before escaping into the FTO substrate. Assuming that grain boundaries in BVO impede transport and considering only that the crystallite size increases in the order noMo/U < Mo/U < noMo/T ≈ Mo/T, we would anticipate the textured films to show the best charge transport, followed by the Mo/U films and then the noMo/U films. However, crystallite size is expected to be only one of several factors that determine the efficiency of charge transport in these films.

Table 1 BVO crystallite sizes from Scherrer XRD analysis

	XRD reflection/crystallite size (nm)						
Sample	(101)	(011)	(004)	(204)	(024)	(031)	Average
noMo/U	37	37	35	29	29	38	34 ± 4
Mo/U	45	46	47	40	40	37	43 ± 4
noMo/T	51	51	59	42	42	36	47 ± 8
Mo/T	50	50	60	45	45	39	48 ± 7

Our simple, single-step spin coating procedure yields phase-pure, nanoporous, uniform, optically perfect, mechanically robust, bright yellow BVO films as thick as ~500 nm over large areas (see photo of a 9 in^2 film in Fig. 1g). Optical transmission

Published on 11 February 2016. Downloaded by University of California - Irvine on 11/02/2016 18:07:40.

and reflection data acquired with an integrating sphere were used to determine the absorbance spectra for the four types of BVO films on FTO-coated glass substrates (Fig. 1h). All of the films have an apparent absorption onset of 480–490 nm (2.53–2.58 eV). Tauc plots show an indirect transition at 2.48–2.52 eV and a direct transition at 2.63–2.69 eV, in agreement with recent reports that BVO is an indirect band gap semiconductor (Fig. S4, ESI†).[6,7] As mentioned above, we attribute the larger absorbance of the textured films mostly to their lower porosity, but the optical anisotropy of BVO, which is predicted to yield particularly strong absorption of photons incident along the *c*-axis,[7] may also contribute to the higher overall absorbance of these films.

Photoelectrochemical sulfite oxidation

The photocurrent density of a photoelectrolysis cell utilizing a single photoelectrode can be conveniently expressed as $J = J_{max} \times \eta_{abs} \times \eta_t \times \eta_{rxn}$, where J_{max} is the maximum photocurrent possible for a given absorber material (6.2–7.5 mA cm^{-2} for $BiVO_4$ based on its band gap of 2.4–2.5 eV) and η_{abs}, η_t, and η_{rxn} are the overall, spectrally integrated quantum efficiencies for light absorption, charge transport to the solid–electrolyte interfaces at which redox reactions occur, and charge transfer reactions across the solid–electrolyte interfaces (preferably to form only the desired products). Although η_t and η_{rxn} are not rigorously independent quantities, they provide useful estimates of bulk recombination and surface recombination, respectively. In general, all three quantum efficiencies depend on photon wavelength, so $J = q\int\Phi(\lambda)\eta_{abs}(\lambda)\eta_t(\lambda)\eta_{rxn}(\lambda)d\lambda$, where $\Phi(\lambda)$ is the spectral photon flux of the incident light (photons s^{-1} m^{-2} nm^{-1}), q is the electron charge, and λ the photon wavelength. When $\eta_t = \eta_{rxn} = 1$, we have $J = J_{max} \times \eta_{abs} = J_{abs}$ (the "absorption-limited photocurrent"), which is typically calculated for a given electrode using the standard AM1.5G solar spectral photon flux, $\Phi_{AM1.5G}$.

We first tested the ability of the four types of BVO electrodes to carry out the anaerobic photoelectrochemical oxidization of sulfite ion (SO_3^{2-}) to sulfate (SO_4^{2-}) and/or dithionate ($S_2O_6^{2-}$):[58]

$$SO_3^{2-} + 2h^+ + H_2O \rightarrow SO_4^{2-} + 2H^+ \quad E^\circ_{ox} = +0.10\ V$$

$$2SO_3^{2-} + 2h^+ \rightarrow S_2O_6^{2-} \quad E^\circ_{ox} = -0.04\ V$$

Sulfite has been used as a hole scavenger for BVO by Ye *et al.*[28] and later by others.[8–10,17,18,31,34,41,42,50] We chose sulfite as a hole scavenger because it is reported to undergo fast oxidization by photogenerated holes at the surface of BVO with $\eta_{rxn} \sim 100\%$, thereby enabling investigation of the photoelectrochemical properties of BVO electrodes without complications from slow surface reactions and surface recombination.[9,18,42] Using sulfite also allows us to compare our results with the largest body of previous work. Our tests of H_2O_2 and methanol as alternative hole scavengers showed that sulfite gives the most ideal current–voltage behavior: H_2O_2 has nearly the same magnitude of anodic photocurrent as sulfite but much larger, less ideal cathodic and anodic dark current, while methanol shows significantly smaller photocurrent and a much more anodic onset potential, indicating that methanol is not suitable as a fast hole scavenger for these BVO films (Fig. S5, ESI†). We are not aware of any direct measurement proving that $\eta_{rxn} \sim 100\%$ for sulfite oxidation on BVO. However, the assumption $\eta_{rxn,sulfite} \sim 100\%$ is well supported by indirect evidence, mainly (i) studies showing that BVO electrodes outfitted with oxygen evolution catalysts have photocurrents for water oxidation that approach but do not exceed the photocurrents for sulfite oxidation,[9,18,34,42] and (ii) the absence of the type of current transients under chopped illumination that are attributed to hole accumulation and recombination near the electrode surface.[21,42] In this paper, we assume $\eta_{rxn,sulfite} = 100\%$ and negligible current doubling by sulfite.[59]

Fig. 2 shows three-electrode current–voltage (*J*–*V*) and external quantum efficiency (EQE) results for sulfite oxidation (0.1 M Na_2SO_3 in 0.5 M aqueous phosphate buffer, pH 7.0) averaged over six devices (see Experimental). Measurements were performed with 1 sun (100 mW cm^{-2}) AM1.5G illumination incident either from electrolyte to electrode ("EE" illumination) or from substrate to electrode ("SE" illumination). As shown in Fig. 2a and d, the noMo/U electrodes (red traces) have a photocurrent onset at ~0.34 V_{RHE} and the smallest photocurrent in both EE and SE illumination (reaching 0.09 and 0.18 mA cm^{-2}, respectively, at 1.23 V_{RHE}). The photocurrent onset is ~0.2 V positive of the

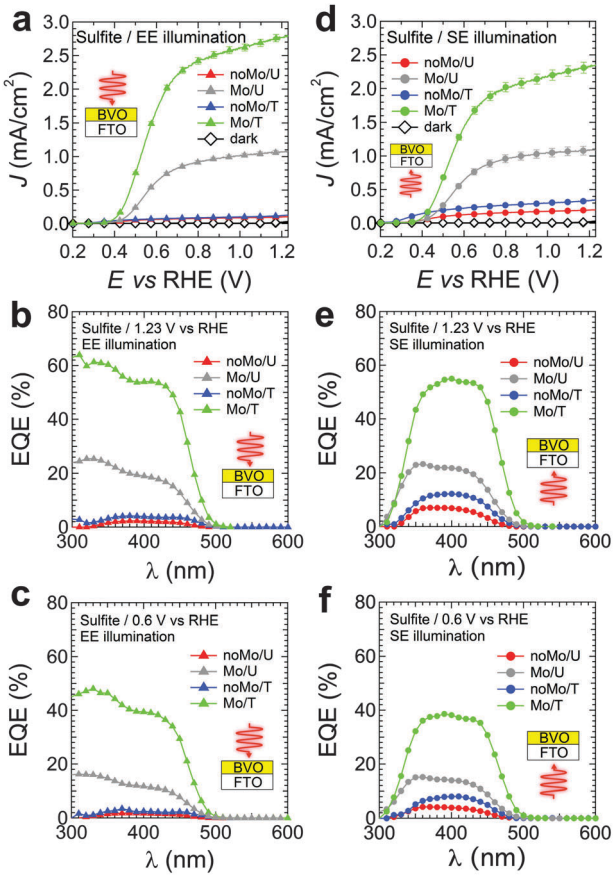

Fig. 2 Current–voltage (*J*–*V*) and external quantum efficiency (EQE) performance of BVO electrodes for sulfite oxidation. (a) Dark and illuminated *J*–*V* and (b) EQE curves at 1.23 V_{RHE} and (c) 0.6 V_{RHE} under EE illumination (*i.e.*, light incident through the electrolyte). (d–f) The analogous data for SE illumination (*i.e.*, light incident through the substrate).

Published on 11 February 2016. Downloaded by University of California - Irvine on 11/02/2016 18:07:40.

flatband potential of 0.13 V_{RHE} that we measured for these films by spectroelectrochemistry (Fig. S6, ESI†).[60] This flat band potential is close to the values typically reported for BVO.[9,34,56] The noMo/T devices (blue traces) have a significantly better photocurrent onset (0.25–0.27 V_{RHE}) and slightly higher photocurrents at 1.23 V_{RHE} (0.11 and 0.32 mA cm^{-2} in EE and SE illumination, respectively) than the noMo/U devices. Untextured electrodes made from ink spiked with 2 at% Mo show much larger photocurrents (1.1 mA cm^{-2} at 1.23 V_{RHE} for both EE and SE illumination) but also a worse onset of 0.43–0.44 V_{RHE} (gray traces). Phase-pure monoclinic Mo/U electrodes made from solutions containing 1% and 3% Mo were also tested but showed lower photocurrent and fill factor, so we used only 2% Mo solutions to make the Mo/U and Mo/T electrodes discussed in the rest of this paper.

The Mo/T electrodes (green traces) outperform the other three film types in both EE and SE illumination, showing (in EE illumination) J = 2.8 mA cm^{-2} at 1.23 V_{RHE} and 1.7 mA cm^{-2} at the relatively low bias of 0.6 V_{RHE}, a photocurrent onset at 0.41 V_{RHE}, and good fill factor. At a given bias, the EE photocurrent of an average Mo/T film is ~2.6 times better than that of a Mo/U film and ~26 times better than a noMo/T film. Our champion Mo/T electrodes show J = 3.1 mA cm^{-2} and 2.5 mA cm^{-2} at 1.23 V_{RHE} under EE and SE illumination, respectively, onset potentials of 0.34–0.37 V_{RHE}, and fill factors of ~0.51, indicating a fairly low rate of carrier recombination within the electrode at low bias (Fig. S7, ESI†). This sulfite oxidation activity is among the best reported for plain BVO photoanodes (those without heterojunctions, composition tuning, or catalysts).[8,9,18,34,41,42] The higher photocurrent under EE illumination is particularly notable because BVO electrodes usually have better SE than EE performance due to inefficient electron transport and the longer average transit distance for photogenerated electrons in the EE geometry.[8,9,24,32,34,42] We show below that the overall, spectrally integrated internal quantum efficiency of these Mo/T electrodes for sulfite oxidation at the OER potential (IQE = $\eta_t = J/J_{abs}$) is 70 ± 5%, limited by hole transport, and that the difference between the EE and SE photocurrents is due primarily to absorption losses in the FTO-coated glass substrate in the SE geometry. Recently, Seabold *et al.* reported very similar results to our own – including a total IQE as high as 90% and larger photocurrent under EE than SE illumination – using 100–300 nm thick Mo:BVO films with a nanoporous morphology comparable to our films but without [001] texture.[18] The maximum power point of our Mo/T devices occurs at 0.63 V_{RHE}, which is sufficiently cathodic for reasonable current matching with existing photocathodes in tandem solar fuel devices. Work is ongoing to shift the maximum operating point to more negative potentials (~0.4 V_{RHE}) to better match photocathodes such as p-Si.

EQE data were acquired at 1.23 V_{RHE} and 0.6 V_{RHE} in both illumination directions (Fig. 2b, c, e and f). The onset of the EQE response for Mo/T and Mo/U films is at somewhat longer wavelength (~515 nm, or 2.41 eV) compared to that of the Mo-free films (~500 nm, or 2.48 eV), perhaps as a result of Mo-induced band tailing or band gap narrowing. Above the band gap, the EQE of the Mo/T and Mo/U films rises quickly and then either levels off below 350 nm (for EE illumination) or peaks before falling nearly to zero by ~300 nm, where the FTO substrate absorbs strongly (for SE illumination). The Mo/T electrodes show the highest peak EQE of ~61% at 1.23 V_{RHE} and ~48% at 0.6 V_{RHE} in EE illumination. Integrating the EQE at 1.23 V_{RHE} over the standard AM1.5G spectrum gives a photocurrent of 2.5 mA cm^{-2}, ~12% less than the value of 2.8 mA cm^{-2} measured in J–V data. The other three film types show lower EQE values. For all films, the measured photocurrent density is up to 40% larger than the value obtained from the EQE spectrum. The difference between J–V and EQE data is bigger for Mo/U films (30–40%) than Mo/T films (0–20%). This type of systematic difference can result from the much higher irradiance used in J–V measurements (100 mW cm^{-2}), which can fill traps and increase the carrier mobility and photocurrent of nanocrystalline electrodes[61] relative to EQE data that are usually acquired using low-power monochromatic light (2–200 μW cm^{-2} in our case) without background light bias. However, we find that EQE spectra of Mo/T films acquired under 0.3 sun white light bias are nearly identical to spectra obtained without light bias (Fig. S8, ESI†), showing that trap filling and other intensity-dependent effects are not responsible for the difference between the J–V and EQE data observed here. J–V plots measured as a function of light intensity show that the photocurrent of these electrodes increases linearly with light intensity up to at least 1 sun (Fig. S8, ESI†), further ruling out any significant irradiance dependence. A second common source of deviation between J–V and integrated EQE data is mismatch between the AM1.5G spectrum and the actual spectral output of the solar simulator. To quantify our spectral mismatch, we carefully measured the absolute spectral irradiance of our solar simulator at the sample position using a fiber-coupled spectrometer calibrated with a radiometric calibrated light source (see Experimental). Surprisingly, we find that the photon flux of our solar simulator is actually ~12% smaller than that of the AM1.5G spectrum over the relevant range of wavelengths for BVO (300–515 nm; Fig. S9, ESI†). Integrating the product of the EQE and the actual spectral photon flux of the solar simulator gives an EE photocurrent for the Mo/T films of only 2.2 mA cm^{-2}, even less than the 2.5 mA cm^{-2} calculated using the AM1.5G standard and in worse agreement with the value from J–V data (2.8 mA cm^{-2}). Since the EQE spectra of these films are independent of light intensity (Fig. S8, ESI†), integrating the EQE with the measured solar simulator spectral photon flux should give the same photocurrent as a J–V plot acquired with the same light source, but this is not the case for our samples. At this time we cannot explain why the J–V and EQE data disagree. We note that reasonable agreement between J–V and EQE data (to within ~10%) is rare in the BVO literature: large discrepancies of 25–50% are common, while only a few examples of good J–V and EQE agreement are known to us.[8,54]

Charge transport efficiency of the highest-performance (Mo/T) electrodes

We estimated the charge transport efficiency $\eta_t(\lambda)$ and internal quantum efficiency (IQE) of Mo/T electrodes for sulfite oxidation ($\eta_t(\lambda)$ = IQE(λ) = EQE(λ)/$\eta_{abs}(\lambda)$) by combining EQE data acquired at 1.23 V_{RHE} with absorptance spectra (*i.e.*, $\eta_{abs}(\lambda)$) obtained with an integrating sphere. EQE, absorptance, and the resulting $\eta_t(\lambda)$ data are shown in Fig. 3 for electrodes with BVO

Published on 11 February 2016. Downloaded by University of California - Irvine on 11/02/2016 18:07:40.

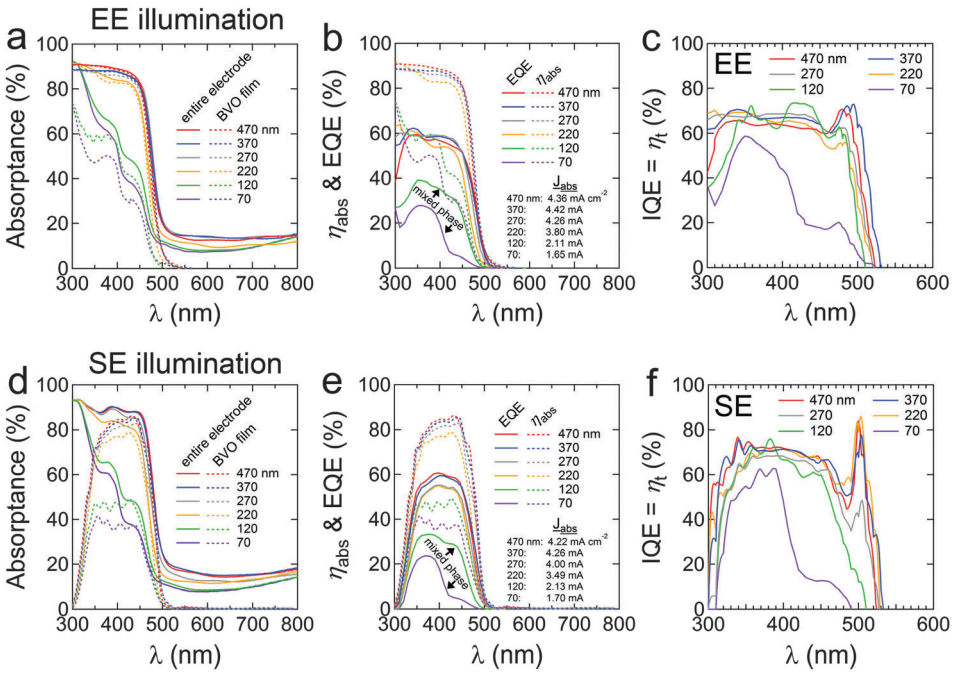

Fig. 3 IQE plots for sulfite oxidation by Mo/T electrodes as a function of BVO film thickness (70–470 nm) and illumination direction. (a–c) For EE illumination. (d–f) For SE illumination. (a and d) Plots of total electrode absorptance from integrating sphere measurements (solid traces) and absorptance of only the BVO film as determined from an optical transfer matrix model[62] of the electrode stack (dashed traces). See Experimental for modeling details. (b and e) Plots of experimental EQE (at 1.23 V_{RHE}, solid traces) and modeled BVO layer absorptance ($\eta_{abs}(\lambda)$, dashed traces). Inset is J_{abs} for each electrode, determined by integrating the product of $\eta_{abs}(\lambda)$ and the AM1.5G solar spectrum. Note that the two thinnest films are mixed-phase tetragonal and monoclinic $BiVO_4$ according to XRD (see Fig. S11, ESI†). (c and f) IQE plots (IQE(λ) = $\eta_t(\lambda)$ = EQE(λ)/$\eta_{abs}(\lambda)$). The peak at 480–500 nm in some of the plots is an artifact of taking the ratio of two similar and rapidly changing curves. The dip at ~300 nm in the SE data is another such artifact. See Fig. S12 (ESI†) for integrating sphere optical data of all films, Fig. S13 (ESI†) for SEM images of the films, and Fig. S14 (ESI†) for optical data of a clean FTO-coated glass substrate.

film thicknesses from 70 to 470 nm (the largest range of thicknesses we could make in a single spin coat step). Film thickness was varied by changing the spin coating speed and adjusting solvent ratios while leaving the ink composition and all other film processing conditions constant (see Experimental). The absorptance spectrum of each electrode is a convolution of $\eta_{abs}(\lambda)$ of the BVO film (*i.e.*, the light harvesting efficiency) plus absorption losses in the FTO substrate. Accurate deconvolution of the BVO and substrate absorptance is needed to determine $\eta_{abs}(\lambda)$, J_{abs}, and $\eta_t(\lambda)$ for each electrode, but this cannot be achieved by applying a simple correction factor to account for FTO absorption because interference effects are usually important in such optically thin multilayer dielectric stacks. To account for thin-film interference effects, it is better to use an optical model to explicitly determine the absorptance of each BVO film.

We fit the measured absorptance spectrum of each electrode using a 1D transfer matrix model[62] (see Experimental) to extract the absorptance due only to the BVO layer, thereby allowing an accurate estimation of $\eta_{abs}(\lambda)$, J_{abs}, and $\eta_t(\lambda)$ in each case. The model shows that absorption by BVO accounts for nearly the entire measured absorptance above the BVO band gap (λ < 480 nm) when relatively thick (>200 nm) films are measured in EE conditions (Fig. 3a). In this case, the electrode absorptance and BVO absorptance are equal to within a few percent. Thinner films in EE illumination show substantial absorption by the substrate that increases with shorter wavelength, such that the BVO absorptance is only a fraction of the overall absorptance throughout the spectrum (Fig. 3a). In SE illumination, there is significant absorption by the substrate for all BVO thicknesses. As expected, substrate absorption increases for λ < 380 nm and drives BVO absorptance to zero in the UV, resulting in mesa-shaped absorptance spectra for SE light (Fig. 3d). Fig. S10 (ESI†) shows modeling results for electrodes with 250 nm ("thick") and 100 nm ("thin") BVO films in both illumination geometries.

Taking the ratio of EQE(λ) to $\eta_{abs}(\lambda)$ (Fig. 3b and e) gives $\eta_t(\lambda)$ (*i.e.*, IQE(λ)) for each Mo/T electrode, plotted in Fig. 3c and f for EE and SE illumination, respectively. The most striking feature of the data is that the IQE(λ) of the thicker films (≥220 nm) is independent of both film thickness and illumination direction (IQE(λ) is 63–72% and flat in all cases). This is possible only if electron transport is efficient for all films and hole transport limits the photocurrent. If electron transport were to limit performance, the IQE and photocurrent should be larger in SE than EE illumination and smaller for thicker films, which is not observed. We therefore conclude that transport of holes limits the photocurrent of our Mo/T BVO films. Films thinner than ~125 nm show significantly lower IQE. We attribute the lower IQE to the presence of tetragonal $BiVO_4$ (PDF # 00-014-0133) in the thinner films (Fig. S11, ESI†), which apparently degrades IQE *via* either poor η_t or η_{rxn}.[63] The thinnest films (70 nm) have the largest fraction of tetragonal BVO and the lowest IQE. We believe that the 70 and 120 nm films would show at least the

This journal is © The Royal Society of Chemistry 2016

Published on 11 February 2016. Downloaded by University of California - Irvine on 11/02/2016 18:07:40.

same IQE as the thicker films if they were phase-pure monoclinic BVO rather than a monoclinic/tetragonal phase mixture. Although integrating the EQE data in Fig. 3b suggests that the 370 and 470 nm films should have the highest 1 sun photocurrent ($J \approx 2.89$ mA cm^{-2}), the 220 nm films perform the best in J–V measurements (Fig. S15, ESI†), which is another example of the common discrepancy between J–V and EQE data for BVO.

Analysis of sulfite oxidation performance of the different BVO films

We demonstrated in the previous section that peak $\eta_t(\lambda)$ of our highest-performance (Mo/T) electrodes is 60–70% and limited by hole transport. The finding that hole transport limits the photocurrent may seem surprising given the small diameter of the rod-like particles in our films (45–70 nm) compared to reported values of the hole diffusion length $\left(L_p = \sqrt{D_p \tau_p}\right)$ of 70–200 nm in various BVO samples.[14–17] However, it is important to consider that L_p is not an immutable material parameter, but can vary by orders of magnitude (*e.g.*, from 10^{-7}–10^{-2} m in silicon) depending on the crystallinity, bulk defect content, and surface properties of a material that affect carrier mobility and lifetime. L_p of our films could easily be smaller than 70–200 nm. Moreover, to achieve $\eta_t \sim 100\%$ solely by diffusion, the diffusion length must be many times longer than the largest carrier transit distance. In the absence of substantial band bending within the BVO, the probability for a photogenerated hole to escape bulk recombination is proportional to e^{-x/L_p}, where x is the distance a given hole must travel to reach the BVO surface. We estimate that L_p must be at least 6 times the particle radius (or >210 nm for our films) to enable quantitative (>95%) hole collection by diffusion alone (assuming the simplest case of a laterally uniform generation rate in the particles). Only ~81% (~65%) of the holes would reach the BVO surface if L_p were equal to the particle diameter (radius). Thus, if band bending is negligible, a hole diffusion length of just 30–40 nm can explain the 60–70% hole transport efficiency of our Mo/T films. L_p could be even smaller if band bending is substantial because then the electric field in the depletion layer can be strong enough to separate carriers and drive holes to the BVO surface. Using a simple nanocrystal Schottky junction model, we estimate that band bending in our ~70 nm diameter BVO nanoparticles is significant only when the electron density is higher than $\sim 1 \times 10^{17}$ cm^{-3}. At a free carrier density of 1×10^{17} cm^{-3}, the depletion layer width (~175 nm at 0.6 V_{RHE} and ~260 nm at 1.23 V_{RHE}) is much larger than the particle radius and the potential difference between the center and surface of a particle is too small (~20 mV) to efficiently separate carriers at room temperature. With increasing carrier density the depletion layer thins ($\propto n^{-1/2}$) and the potential difference and maximum electric field increase in magnitude. Since the carrier density in BVO films may easily be higher than 10^{17} cm^{-3}, we think it is likely that at anodic potentials drift plays an important role in charge transport, which would enable efficient hole collection even for quite short L_p. Our results imply that the hole diffusion length in these BVO films is shorter than 40 nm.

The main trends in the J–V and EQE data of Fig. 2 are readily understood. The increase in photocurrent and EQE in the order noMo/U < noMo/T < Mo/U < Mo/T is due to progressively better charge transport. Differences in light absorption between the films are relatively insignificant (J_{abs} differs by less than 45%) and cannot account for the much larger differences in photocurrent. The noMo/T films show up to twice the photocurrent of the noMo/U films, but their absolute performance is poor, suggesting that carrier collection is improved but still inefficient in textured films made without Mo. Both the noMo/U and noMo/T films show 4–5 times higher peak EQE in SE than EE illumination, which is good evidence that electron transport is inefficient in these films. This is because, even in the presence of strong optical interference effects,[62] the performance of electrodes limited by electron transport should be best in SE illumination since electrons are generated closer to the FTO substrate and thus have a shorter average transit distance when light is incident though the substrate than when it is incident from the opposite side of the film. In contrast, the average travel distance for holes is about equal in SE and EE illumination because the BVO/water interface is distributed somewhat uniformly throughout the volume of the nanoporous BVO films, so the hole transport efficiency should depend only weakly on illumination direction. Although absorption losses in FTO can decrease J_{abs} in SE illumination by 5–10% (*e.g.*, see Fig. 3), the higher EQE from better electron collection in the SE geometry can dwarf the reduction due to the slightly smaller film absorptance.

A comparison of the Mo/U and Mo/T films makes it clear that Mo addition mostly improves electron transport, while texturing mostly improves hole transport. The Mo/U films have six times higher photocurrent than noMo/U films and strikingly similar performance in SE and EE illumination, with nearly identical J–V curves (J = 1.1 mA cm^{-2} at 1.23 V_{RHE}), integrated EQE (~0.8 mA cm^{-2}), J_{abs} (~2.65 mA cm^{-2}), and $\eta_t \sim 42\%$ in both illumination geometries. The lack of dependence on illumination direction suggests that electron transport is efficient and that poor hole transport limits the photocurrent of the Mo/U electrodes. We therefore conclude that Mo addition mostly improves electron transport in BVO films. This conclusion is consistent with the discussion above and previous reports (see following section). Meanwhile, Mo/T films have 2–3 times higher photocurrent than Mo/U films and slightly better performance in EE than SE illumination, with ~20% higher EE photocurrent in J–V measurements (2.8 mA cm^{-2} *versus* 2.34 mA cm^{-2} at 1.23 V_{RHE}) and 10% higher EE value of the integrated EQE (2.5 mA cm^{-2} for EE light *versus* 2.3 mA cm^{-2} for SE light). The photocurrent of the Mo/T electrodes is higher in EE than SE conditions because of lower absorption losses in the FTO substrate and more absorption in the BVO film (J_{abs} = 3.8 mA cm^{-2} in EE light but only 3.49 mA cm^{-2} in SE light; see Fig. 3). Indeed, higher EE photocurrent should be a distinguishing characteristic of quantitative electron collection from BVO films on transparent conducting substrates such as FTO/glass, as previously noted by Seabold *et al.*[18] Since electron transport is efficient in both the Mo/U and Mo/T films, we attribute the significantly higher photocurrent of the Mo/T electrodes mostly to improved hole transport, which increases $\eta_t(\lambda)$ from ~40% to 60–70%.

Published on 11 February 2016. Downloaded by University of California - Irvine on 11/02/2016 18:07:40.

Possible mechanisms by which hole transport is enhanced in the textured films are discussed in the following section.

To summarize, the trends in photocurrent and EQE in Fig. 2 are a result of progressively better charge transport in the series noMo/U < noMo/T < Mo/U < Mo/T. Comparing the magnitude of the photocurrent and the relative performance of each type of BVO film in EE and SE illumination shows that Mo addition primarily improves electron transport, while texturing mostly improves hole transport. Thus, noMo/U films have the lowest photocurrent and $J_{SE} \gg J_{EE}$ because both electron and hole transport are poor. Hole transport is improved in noMo/T films, but electron transport is still limiting and so $J_{SE} \gg J_{EE}$. Conversely, Mo/U films have efficient electron transport (evidenced by $J_{SE} \sim J_{EE}$) but still poor hole transport, resulting in only modest photocurrent. Mo/T films combine efficient electron transport ($J_{SE} < J_{EE}$) with significantly improved hole transport (peak $\eta_t(\lambda)$ = 60–70% and total $\eta_t = 70 \pm 5\%$ at 1.23 V_{RHE}) and show the highest photocurrent. The electron and hole transport performance remains unchanged for Mo/T films up to at least 470 nm thick (Fig. 3).

The charge transport efficiency of our Mo/T films is among the highest yet reported for single-component BVO electrodes. Higher η_t values of ~90% at 1.23 V_{RHE} have been reported in two recent studies,[9,18] but these values appear to be misestimated. Reference 18 may overestimate η_t by underestimating J_{abs} in two ways: (i) neglecting light absorption below 350 nm, which is sufficient to increase J_{abs} by ~0.3 mA cm^{-2} and lower η_t from ~90% to ~82%, and (ii) using a simple correction factor rather than a model to remove the substrate absorptance under EE illumination, which tends to underestimate the BVO absorptance and thus overestimate η_t. We cannot determine exactly how much η_t has been overestimated because the procedure used to remove the substrate absorptance is not described in that paper. However, given the above arguments as well as the reported photocurrent (3.1 mA cm^{-2}) and film thickness (300 nm), it is very likely that η_t is closer to ~70% than ~90%, and therefore quite similar to our result. Reference 9 apparently misestimates J_{abs} in two ways. First, the electrode absorptance from 380–650 nm is used to calculate J_{abs}, but this spectral region misses a substantial amount of AM1.5G light that is absorbed by BVO (300–380 nm, worth ~0.36 mA cm^{-2} for these electrodes in the SE geometry) and includes a significant amount of sub-bandgap light that is not absorbed by BVO (520–650 nm, worth ~0.4 mA cm^{-2}). These two errors nearly cancel. The measured photocurrent of ~4.5 mA cm^{-2} (at 1.23 V_{RHE}) is ~100% of both the uncorrected and corrected J_{abs} (4.45 and 4.41 mA cm^{-2}, respectively), not ~90% as claimed in that paper. Moreover, accounting for the absorptance of the FTO substrate in the electrode stack under SE illumination lowers J_{abs} by ~10%, resulting in an unphysical η_t of ~110%. This implies significant spectral and/or intensity mismatch between 1 sun AM1.5G light and the output of the solar simulator used in the measurements, which calls the reported η_t value into question.

Mechanism of photocurrent enhancement by Mo addition and texturing

We now briefly discuss why the addition of molybdenum improves the electron transport of BVO photoelectrodes. The usual explanation is that Mo is a donor that increases film conductivity, which in turn enhances the photocurrent in some way. There are two problems with this explanation. First, although atomistic models predict that substitutional molybdenum on a vanadium site (Mo_V) is a shallow donor in BVO,[27,33] the bulk of the experimental data shows that doping by Mo is very inefficient, with a donor efficiency (*i.e.*, the number of free carriers contributed per impurity atom) of <1% at room temperature. A donor efficiency of only 0.005% was reported in BVO single crystals containing 0.6% Mo (8×10^{19} cm^{-3}).[17] Mott–Schottky measurements of BVO thin films show that adding even higher levels of Mo ($1–5 \times 10^{20}$ cm^{-3}) results in only small increases in the free electron density (by 2–10×, with an absolute increase of 10^{17}–10^{18} cm^{-3}).[28,29,31,34,40–42] This low donor efficiency indicates that Mo is either a deep donor (perhaps 125–250 meV below the conduction band edge) or a shallow donor that is almost completely auto-compensated by acceptor defects (most likely bismuth vacancies) that form along with the Mo_V centers.[17,64–68] In either case, the small decrease in film series resistance upon Mo addition is not expected to have a significant effect on majority carrier transport or photocurrent. The second problem with the notion that Mo enhances BVO photocurrent by acting as a dopant is that dopants are defects that, at least in bulk semiconductors, shorten the diffusion length of minority and majority carriers and degrade photocurrent. To improve the photocurrent, the Mo impurities must decrease recombination in some way. One possibility is that the small Mo-induced increase in electron density thins the surface depletion layer enough to significantly improve electron–hole separation and collection by drift.[31] This mechanism is well known, *e.g.*, in hematite photoelectrodes.[69,70] Another possibility is that Mo improves the electron diffusion length and device photocurrent by passivating traps and recombination centers at grain boundaries and perhaps also at the BVO/electrolyte and BVO/FTO interfaces. Both depletion layer thinning and surface/interface passivation are physically reasonable mechanisms by which Mo may act to enhance the photocurrent of BVO thin-films. Either mechanism can in principle account for the 4-fold increase in electron mobility and 200-fold increase in electron lifetime recently reported for Mo:BVO films by Seabold *et al.*[18]

Next we consider why the textured BVO films show enhanced hole transport. It is conceivable that the enhanced performance is due to the crystallographic texturing itself or to some other difference between textured and untextured films. To better understand the mechanism of improved photocurrent in textured films, we studied the impact of texturing on the microstructure, crystallinity, and electronic defect concentration of the BVO films. We first elucidated the nature of the apparent {00*l*} out-of-plane crystallographic texture of the Mo/T films. Fig. 4a compares XRD patterns of a typical Mo/T film on FTO obtained in grazing incidence (GIXRD, as in Fig. 1e) and conventional $\theta/2\theta$ geometries. The significantly higher relative intensity of the 004 reflection in the $\theta/2\theta$ scan indicates strong preferred orientation of the {00*l*} planes of BVO parallel to the plane of the substrate. Also, a $\theta/2\theta$ scan of the powder scraped from several Mo/T films lacks any preferred orientation and is close to an isotropic powder

 This journal is © The Royal Society of Chemistry 2016

Published on 11 February 2016. Downloaded by University of California - Irvine on 11/02/2016 18:07:40.

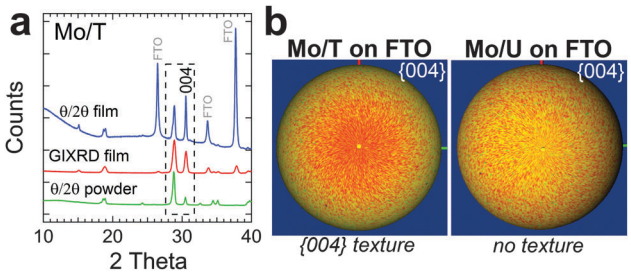

Fig. 4 XRD analysis of textured BVO films. (a) GIXRD and $\theta/2\theta$ scans of a Mo/T film on an FTO substrate, as well as a $\theta/2\theta$ scan of powder collected from several Mo/T films. The 004 peak is significantly enhanced in the $\theta/2\theta$ film pattern but shows no enhancement in the powdered sample relative to the isotropic powder reference file. The strong FTO peaks in the $\theta/2\theta$ film data result from greater penetration of X-rays into the sample in this geometry. (b) {004} pole figures of Mo/U and Mo/T films on FTO substrates. The film normal is perpendicular to the plane of the figure.

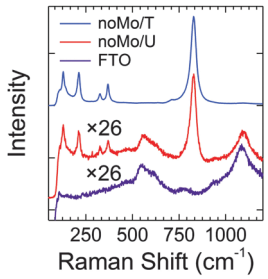

Fig. 5 Raman spectra of textured and untextured films. Typical spectra of a noMo/T film and a noMo/U film, along with the spectrum of a clean FTO substrate (no BVO) for reference. The latter two spectra are multiplied by a factor of 26 and offset. Acquisition conditions: 532 nm, 5% power, 10 s integration, normal incidence and collection. See Fig. S18 (ESI†) for Raman data of all four film types on the same scale.

pattern, indicating that the Mo/T films are truly textured rather than merely composed of highly anisotropic grains (such as long nanorods).

We acquired {004} pole figures of Mo/U and Mo/T films to better characterize the film texture. A pole figure is a hemispherical stereographic projection of a specific crystal plane normal (or pole) of each of a representative number of crystallites in a sample. As shown in Fig. 4b, Mo/T films on FTO show substantial {004} texture normal to the film surface, while Mo/U films are practically untextured. Interestingly, the {004} normal changed from predominantly out-of-plane to in-plane orientation for Mo/T films grown on quartz instead of FTO-coated glass substrates (Fig. S16, ESI†). This result indicates that the substrate can direct the nature of the texturing in these BVO films.

Given that the *c*-axis is reported to be the direction of highest resistivity (*i.e.*, lowest mobility) in BVO crystals,[17,71] we expect *c*-axis texture in nanoporous BVO films to result in better hole transport but worse electron transport compared to untextured films. Substantially better hole collection due to less *c*-axis character in the hole transit path could account for the higher photocurrent of Mo/T films, but only if the lower electron mobility within the BVO grains has an insignificant negative impact on the electron collection efficiency. Indeed, it is likely that electron transport is limited by slow transfer between the multiple BVO grains in the transit path, such that the mobility within grains is unimportant and electron collection is not degraded by the texture. Texturing may also result in more benign grain boundaries, stronger surface electric fields, and other favorable changes that improve both electron and hole collection.

In addition to the texture itself, we investigated several other notable differences between textured and untextured films as possible causes of the enhanced photocurrent of Mo/T photoanodes. We found that the textured films have remarkably more intense Raman spectra than the untextured films, but this proved to be an effect of the crystallographic orientation rather than better crystallinity in the textured samples. Using identical acquisition parameters, we observed 26-fold larger Raman peaks from the textured films (noMo/T and Mo/T), with insignificant differences in peak positions and relative peak intensities compared to the untextured films (Fig. 5). The peak intensity difference between textured and untextured films was eliminated when the films were scraped off their substrates and re-measured as random packed powder pellets (Fig. S17, ESI†). Since the intensity of Raman scattering from a crystal depends on the polarization of the incident and scattered light with respect to the crystallographic axes (Raman polarization anisotropy),[72,73] the Raman signal intensity from textured and untextured films is expected to differ. Based on the identical Raman spectra of the powdered noMo/T and Mo/T films, we conclude that the higher Raman signal of the intact Mo/T films is simply a result of crystallographic orientation (texture) rather than evidence of more perfect crystallinity or fewer structural defects in the textured films.

We next used X-ray and ultraviolet photoelectron spectroscopy (XPS and UPS) to characterize the differences in surface composition and valence band electronic structure of the textured and untextured BVO films (see Experimental). XPS survey and individual element core level scans are shown in Fig. S19 and S20 (ESI†). After Shirley background subtraction, the Bi 4f core level peaks Bi $4f_{7/2}$ and Bi $4f_{5/2}$ of all films fit well to single-component Voigt functions with binding energies of 159.2 and 164.5 eV (Δ = 5.3 eV), FWHM values of 0.96 and 0.98 eV, and the expected area ratio of 4 : 3, allowing unambiguous assignment to Bi^{3+}.[74,75] The V 2p core level peaks V $2p_{3/2}$ and V $2p_{1/2}$ have binding energies of 516.8 and 524.4 eV (Δ = 7.6 eV), FWHM values of 0.87 and 2.3 eV, and the expected area ratio of 2 : 1, and are assigned to V^{5+} in BVO.[19,46,74,76] In most of our samples there is no evidence for V^{4+}, which is expected to have a binding energy of 515.5–516.0 eV.[12,74,76] Occasionally we observed a very weak low-binding energy tail at 515.6 eV assignable to V^{4+} (see Mo/U sample in Fig. S20, ESI†). Cooper *et al.* have also reported such a weak V^{4+} signature in BVO XPS data.[12] Rossell *et al.* recently assigned the V $2p_{3/2}$ peak of a commercial BVO powder observed at 516.7 eV to V^{4+},[77] but we believe this assignment is incorrect. Some reduced vanadium may indeed be present at the surface of their samples, but the published spectra are too broad (possibly as a result of a large pass energy) to be certain. Nondestructive synchrotron XPS depth profiling would enable

Published on 11 February 2016. Downloaded by University of California - Irvine on 11/02/2016 18:07:40.

Table 2 $E_F - E_{VBM}$, Φ, E_g, and surface composition of BVO films

Sample[a]	$E_F - E_{VBM}$ (eV)	Φ (eV)	E_g[b] (eV)	Surface [V]/[Bi][c]	Bulk [V]/[Bi][d]
noMo/U	2.32	5.04	2.49 (E); 2.52 (O)	0.43	0.83
Mo/U	2.22	5.03	2.41 (E); 2.51 (O)	0.85	0.84
noMo/T	2.20	4.96	2.49 (E); 2.51 (O)	0.47	0.89
Mo/T	2.21	5.22	2.41 (E); 2.48 (O)	0.52	0.82

[a] All samples UV/ozone cleaned. [b] E = determined from EQE onset, O = determined from optical Tauc plot fit. [c] Determined from XPS. [d] Determined from EDS.

better quantification of the presence and distribution of reduced vanadium species (V^{4+} and V^{3+}) near the BVO surface.

Quantification of the XPS data suggests that all of the films have nonstoichiometric, highly vanadium-deficient surfaces with [V]/[Bi] = 0.43–0.85, compared to [V]/[Bi] = 1 expected for $BiVO_4$ (see Table 2). Our results agree with previous reports that conclude on the basis of XPS data that the BVO surface tends to be significantly vanadium deficient.[24,51,55,77,78] In addition, the anion/cation ratio [O]/([Bi] + [V]) is only 1.65–1.85 (rather than 2), suggesting large oxygen deficiency or the presence of additional metal oxide phases near the surface. This fairly extreme nonstoichiometry indicates that the surface of our BVO films is not $BiVO_4$, but probably a blend of $BiVO_4$ and bismuth-rich, oxygen-deficient phases such as $Bi_2VO_{5.5}$, Bi_2O_3, and $BiVO_{4-\delta}$.[77] To compare the surface [V]/[Bi] ratio from XPS with the total (surface plus bulk) [V]/[Bi] ratio of the films, we performed standardless semi-quantitative energy dispersive spectroscopy (EDS).[79,80] EDS shows a significant but smaller vanadium deficiency than XPS, with [V]/[Bi] = 0.82–0.89 ± 0.1 (Table 2). The XPS and EDS data are consistent with a bismuth-rich, vanadium-deficient surface layer on otherwise stoichiometric BVO grains. Recently it was suggested that the BVO surface may consist of bismuth oxides devoid of vanadium.[77] To test this idea, we used low-energy He^+ ion scattering spectroscopy (LE-ISS) to identify the atoms present on the top surface of a Mo/T film. While the information depth of XPS is 3–10 nm, the information depth of LE-ISS using noble gas ions is limited to the outermost atomic layer of a sample, thus providing ultimate surface sensitivity.[81] The ion scattering data show strong peaks for Bi, O, and V, indicating that the surface of our films is Bi–V–O (possibly plus H, which cannot be detected in our backscattering geometry) rather than bismuth oxides or oxyhydroxides (Fig. S21, ESI†). Molybdenum was detected by XPS but not by EDS or ISS. Quantification of XPS depth profiles (not shown) indicate that the Mo concentration is constant with sputter depth at ~0.6 at% in the Mo/U films and ~0.2 at% in the Mo/T films, but the profiles do not reveal whether the Mo concentration differs between the bulk and the surface of the BVO crystallites. Based on the XRD, XPS, EDS, and ISS results, we conclude that our films are bulk monoclinic $BiVO_4$ with a bismuth-rich, vanadium- and oxygen-deficient surface layer (*e.g.*, a mixture of $Bi_2VO_{5.5}$, Bi_2O_3, and $BiVO_4$), with a Bi–V–O(–H) surface termination. It is important to keep in mind while interpreting the valence band spectra presented below that the surface of these BVO films is something other than $BiVO_4$ and may have a significantly different effective electronic structure and band gap than the film bulk. Atom-resolved scanning transmission electron microscopy and spectroscopy would be useful for determining the detailed atomic structure and composition of the surfaces of BVO photoelectrodes.

X-ray and UV excited valence band spectra show a striking difference between the textured and untextured films, namely a broad peak from occupied states centered 0.65–0.75 eV above the valence band maximum that is about ten times weaker in textured films than untextured films (Fig. 6). Control experiments show that this in-gap peak is independent of both the KOH etch used to make the textured films and the UVO treatment used to clean the samples prior to UPS measurements. Chemically reducing the film surface by *in situ* dosing with atomic hydrogen progressively increased the intensity of the in-gap peak, suggesting that it is related to oxygen vacancies, reduced metal ions, or interstitial hydrogen in the assemblage of $BiVO_4$ and other phases that exist at the film surface (Fig. S22, ESI†). We assign the peak to defect states in the band gap of BVO rather than the valence states of the surface impurity phases. However, from the photoemission spectra alone we cannot determine whether the defects are surface states or bulk defects. If they are bulk defects, these occupied deep gap states should act as efficient recombination centers, and their lower concentration in the textured films could result in better hole transport that accounts for the higher photocurrent we observe from noMo/T and Mo/T samples. Determining why the textured BVO films have a lower concentration of gap states is very difficult. At present we can only say that inks with [V]/[Bi] ≈ 2 somehow

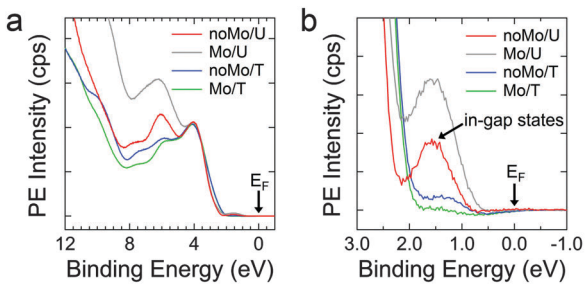

Fig. 6 Ultraviolet photoelectron valence band spectra of textured and untextured films. (a) Overview of the valence band spectra of BVO films cleaned by three cycles of *ex situ* UV/ozone treatment to remove organic contamination. Spectra were aligned with each other at 4 eV. E_F is the Fermi level. (b) Magnified view of the valence band edge showing in-gap states. The in-gap defect peak is significantly larger for untextured films, suggesting a higher defect concentration. The dip below zero counts near ~0.6 eV is an artifact resulting from imperfect numerical subtraction of He I satellites.

 This journal is © The Royal Society of Chemistry 2016

Published on 11 February 2016. Downloaded by University of California - Irvine on 11/02/2016 18:07:40.

result in BVO films with *c*-axis texture, a lower concentration of deep gap states, and higher photocurrent due to better hole transport. We note that several studies have reported that mild reduction by hydrogen annealing[38,82] or electrochemical treatments[24,83] actually improves the photoelectrochemical performance of BVO films, which seems contrary to our results. A separate study of the deep gap states is warranted.

The photoemission spectra provide important additional information about the BVO films, including the position of the surface Fermi level with respect to the valence band maximum ($E_F - E_{VBM}$) and the work function ($\Phi = E_{vacuum} - E_F$). These data are compiled in Table 2 for the four types of BVO films. $E_F - E_{VBM}$ values of 2.2–2.3 eV confirm that all of the films have n-type surfaces, in agreement with the n-type bulk behavior inferred from the *J*–*V* characteristics. This is true as long as the surface layer has a band gap smaller than ~4.6 eV, which seems likely despite the marked surface nonstoichiometry discussed above. The films made with Mo do not show smaller $E_g - (E_F - E_{VBM})$ values than the Mo-free films (as determined using the optical E_g values of the bulk films), indicating that Mo does not substantially increase the free electron density at the surface of these samples (*i.e.*, Mo is not a good donor), which is consistent with the evidence of the low donor efficiency of Mo discussed above. The work function determined from the UPS secondary electron cutoff energy is 5.0–5.2 eV for all films, in good agreement with recent results on BVO films made by chemical vapor deposition.[12]

Photoelectrochemical water oxidation

In addition to sulfite, we also tested the four types of BVO photoelectrodes for their ability to oxidize water. The films were 220 nm thick and bare (no catalyst or surface treatment applied). Fig. 7 shows three-electrode *J*–*V* and EQE results for water oxidation in 1.0 M KH_2PO_4 buffer (pH 7.0) averaged over six devices. As in the case of sulfite oxidation, the Mo/T electrodes demonstrate the highest photocurrent, reaching J = 1.8 mA cm^{-2} under EE illumination and J = 1.1 mA cm^{-2} under SE illumination at 1.23 V_{RHE}. The EQE of the Mo/T films plateaus at 30% under EE light. Since the BVO films photocorrode when polarized anodically (see below), the *J*–*V* data reported in Fig. 7 were acquired quickly (within three minutes after initial illumination). Bubbling was observed from both the BVO and Pt electrodes during these experiments at a rate that increased with the current, consistent with overall water splitting. Comparing the results for sulfite oxidation and water oxidation (Fig. 2 and 7), it is interesting to note that the photoresponse of the Mo/T films is ten times larger than that of the Mo/U films for water oxidation but only three times larger for sulfite oxidation, which suggests that the surface of the Mo/T films is significantly better at transferring holes to water (*i.e.*, higher η_{rxn} for Mo/T than Mo/U films). However, since our films were not coated with a water oxidation catalyst, the photocurrent onset potential is ~0.16 V more anodic and the fill factor is substantially lower for water oxidation than for sulfite oxidation (see comparison in Fig. 8a). This corroborates the relatively sluggish nature of water oxidation on the surface of bare BVO reported in previous studies.[2] Nonetheless, the *J*–*V* and EQE performance of our Mo/T films is among the best reported for BVO electrodes without catalysts,[9,18] showing that these films have efficient carrier transport and fairly good hole transfer to water.

Using the relation $J = J_{abs} \times \eta_t \times \eta_{rxn}$ with $\eta_{rxn,sulfite}$ = 100%, we estimated the overall, spectrally integrated quantum efficiencies for charge transport ($\eta_t = J_{sulfite}/J_{abs}$) and hole transfer to water $\left(\eta_{rxn,water} = \frac{J_{water}}{J_{abs} \times \eta_t}\right)$ for the Mo/T electrodes in EE illumination as a function of applied bias. Fig. 8a compares typical *J*–*V* curves of Mo/T electrodes for sulfite and water oxidation. Fig. 8b shows that η_t determined using the *J*–*V* curve in sulfite electrolyte and J_{abs} = 3.80 mA cm^{-2} (Fig. 3b) is ~45% at 0.6 V_{RHE} and ~74% at 1.23 V_{RHE} (blue curve in Fig. 8b). η_t is 79% at 1.23 V_{RHE} if we use J_{abs} for the absolute spectral photon flux of our solar simulator (3.55 mA cm^{-2}) – which is the actual light source used in the *J*–*V* measurements – rather than J_{abs} for

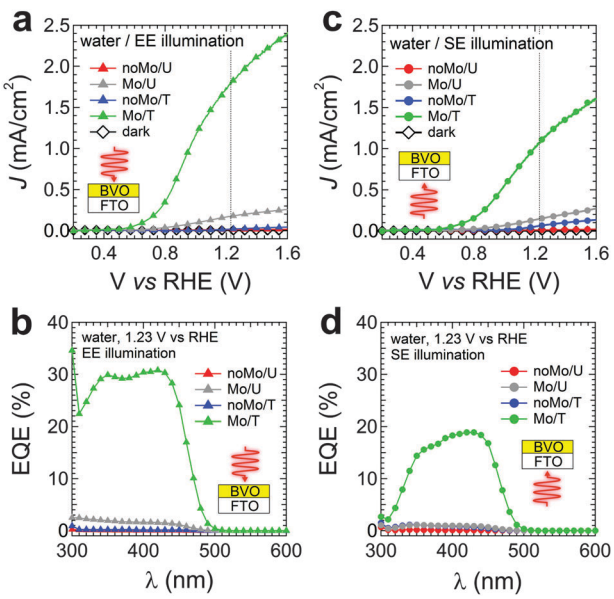

Fig. 7 Current–voltage (*J*–*V*) and external quantum efficiency (EQE) performance of 220 nm thick BVO electrodes for oxidation of water. (a) Dark and illuminated *J*–*V* and (b) EQE curves at 1.23 V_{RHE} under EE illumination. (c and d) The analogous data for SE illumination.

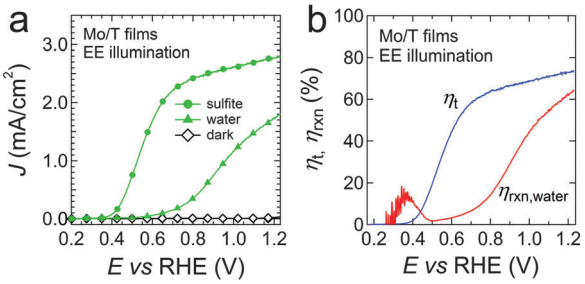

Fig. 8 Determination of the quantum efficiencies for charge transport (η_t) and water oxidation by holes at the BVO surface ($\eta_{rxn,water}$). (a) *J*–*V* plots for sulfite and water oxidation by Mo/T films in the light and dark. EE illumination. (b) η_t and $\eta_{rxn,water}$ as a function of bias. EE illumination. The small peak in $\eta_{rxn,water}$ centered at ~0.36 V is a mathematical artifact.

Published on 11 February 2016. Downloaded by University of California - Irvine on 11/02/2016 18:07:40.

the AM1.5G spectrum (3.8 mA cm^{-2}). Alternatively, determining overall η_t by integrating the product of $\eta_t(\lambda)$ and the AM1.5G spectral photon flux gives a somewhat lower value ($\eta_t \sim 64\%$ at 1.23 V_{RHE}). Given the spread in η_t values determined from *J–V* and EQE data, we can conservatively estimate that $\eta_t = 70 \pm 5\%$ at the OER potential. Assuming that the η_t curve in Fig. 8b is the same for sulfite and water oxidation, we can calculate $\eta_{rxn,water}$ at each bias (red curve in Fig. 8b). We find that $\eta_{rxn,water}$ reaches ~64% at the OER potential. Hole pile up at the BVO surface due to the comparatively slow water oxidation kinetics may cause additional recombination that somewhat reduces η_t during water oxidation, so we believe that our estimate of $\eta_{rxn,water}$ is a lower bound. Regardless, 64% is one of the best reported values of η_{rxn} for water oxidation by a bare $BiVO_4$ photoanode.[9,18] The high $\eta_{rxn,water}$ of these Mo/T films may result from their relatively low density of in-gap defect states, the activity of the particular crystal facets exposed to the electrolyte by the textured films,[84,85] and/or fortuitously fast kinetics for the OER relative to competing processes such as recombination and photocorrosion (see below).

Electrode stability

Finally, we assessed the stability of the bare Mo/T BVO electrodes for sulfite and water oxidation by potentiostatic measurements of the current density under illumination at 1.23 V_{RHE} with constant stirring to avoid mass transport limitations and bubble accumulation. As expected from previous reports,[10,34] the electrodes are fairly stable in sulfite electrolyte at pH 7, showing less than a 10% decrease in current after 14 hours of continuous 1 sun illumination (Fig. 9a). The charge passed through the electrode during this time (~142 C cm^{-2}) is approximately 500 times larger than what is required to oxidize all of the O^{2-} ions in the BVO film to O_2 (~0.29 C cm^{-2} for a 220 nm thick film with a conservative porosity of 10%), showing that essentially all of the observed photocurrent comes from sulfite oxidation rather than BVO photocorrosion. The stability of the electrodes during water oxidation is much worse than for sulfite oxidation, with ~90% decrease in current after only one hour of biased illumination, followed by a much slower decrease in current over the next hour. Post-mortem visual inspection and SEM imaging of the electrodes (Fig. 9b) revealed that most of the BVO film etches away during the two hour test. Control samples held at the OER potential in the dark showed minimal decay in current density, optical extinction, and morphology after even 4 hours of testing (Fig. S23, ESI†), proving that the BVO films are reasonably stable in the dark at pH 7 and that the rapid degradation observed under illumination is due to photoinduced rather than dark corrosion of BVO. The charge passed during the two hour illuminated test (2.38 C cm^{-2}) is at least 8 times larger than the charge needed to completely photoetch the BVO film. Thus, as with sulfite oxidation, it is clear that nearly all of the observed photocurrent in Fig. 7 and 9 is due to water oxidation rather than photocorrosion. The mechanism of BVO photocorrosion in water at near-neutral pH is not yet understood, but seems to begin with preferential dissolution of vanadium near the surface, leaving behind a very bismuth-rich surface layer.[22,51,55] One scenario is that the accumulation of photogenerated holes at the BVO surface causes oxidation of the electrode (*via* oxidation of Bi^{3+} and/or O^{2-}) and its eventual dissolution, while photogenerated electrons pass through the external circuit to produce H_2 at the counter electrode. This process would result in photocurrent. It is also possible that photocorrosion occurs by local redox reactions, perhaps most plausibly the reduction of V^{5+} to V^{4+} coupled with oxidation of bismuth or oxygen to ultimately generate solvated metal complexes and perhaps some insoluble metal oxide by-products. This process would not result in photocurrent in the external circuit. Because as few as ~64% of the holes that reach the BVO surface are used to oxidize water, many photogenerated carriers are available to participate in slow corrosion reactions at the BVO/electrolyte interface. Future work will focus on understanding the reactions responsible for BVO photocorrosion at different pH values and coating BVO films with protective layers and oxygen evolution catalysts[22,54] to achieve simultaneous high performance and stability during water oxidation.

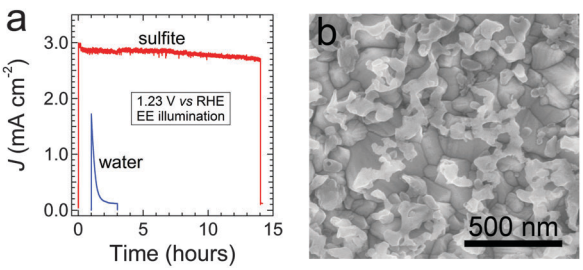

Fig. 9 BVO photoelectrode stability. (a) Typical plots of current density *versus* time for 220 nm Mo/T electrodes performing oxidation of sulfite (red) and water (blue). Conditions: 1.23 V_{RHE}, EE illumination. The light was turned on at time zero and turned off after 14 hours and 2 hours, respectively. The water oxidation data are right shifted by 1 hour for clarity. See Fig. S24 (ESI†) for short-term stability data under chopped illumination. (b) SEM image of an electrode after two hours of water oxidation testing (compare to the un-etched film in Fig. 1d).

Conclusion

We developed a simple spin coating method for making high-quality nanoporous films of monoclinic $BiVO_4$ and used these films to better understand the ability of $BiVO_4$ to absorb light, transport photogenerated carriers, and oxidize sulfite and water in a photoelectrochemical half-cell. BVO films were made with and without molybdenum and [001] out-of-plane crystallographic texture by adjusting the composition of the ink used for film deposition. Mo-containing, textured (Mo/T) films showed significantly higher performance than the three other types of BVO films, with photocurrent and EQE for sulfite oxidation as high as 3.1 mA cm^{-2} and 60% at 1.23 V_{RHE} and 2.5 mA cm^{-2} and 48% at 0.6 V_{RHE} for 220 nm thick films under standard light. By using an optical model of the electrode stack to accurately determine the fraction of electrode absorptance due to the BVO active layer, we estimated a charge transport efficiency of 70 ± 5% for Mo/T films. The fact that IQE(λ) of these films is constant (60–70%) regardless

 This journal is © The Royal Society of Chemistry 2016

Published on 11 February 2016. Downloaded by University of California - Irvine on 11/02/2016 18:07:40.

of illumination direction and film thickness (from 220 nm to at least 470 nm) is strong evidence that electron transport is very efficient and hole transport limits the photocurrent. This IQE behavior is consistent with a hole diffusion length shorter than 40 nm. Comparing the magnitude of the photocurrent and the relative performance of the BVO films in the two illumination directions shows that Mo addition primarily improves electron transport, while texturing mostly improves hole transport. Mo seems to be an inefficient donor in BVO and probably enhances electron transport by thinning the surface depletion layer or passivating traps and recombination centers at grain boundaries and interfaces. Meanwhile, improved hole transport in textured films may stem from more efficient lateral hole extraction due to the texturing itself or the reduced density of a prominent but previously unreported deep gap state observed in photoemission measurements. The photoemission data also show that the films have bismuth-rich, vanadium- and oxygen-deficient surface layers, while ISS indicates a Bi–V–O(–H) surface termination. Increasing the hole transport efficiency of plain Mo/T films from ~70% to ~100% might be achieved in several ways, including more complete passivation of the deep gap states to increase the hole diffusion length, finer nanostructuring of the films to eliminate grain boundaries and shorten the hole transit distance, and tuning the composition of the surface layer to promote the drift of holes to the BVO surface.

Mo/T BVO films without catalyst coatings oxidized water with an initial photocurrent and EQE as high as 1.7 mA cm^{-2} and 30%, respectively, and a hole transfer efficiency to water ($\eta_{rxn,water}$) of at least 64% at the OER potential. Electrode stability during water oxidation is poor, with ~90% loss of photocurrent after 1 hour of illumination at 1.23 V_{RHE}. The photocurrent falls because most of the BVO film etches away after just a few hours of water oxidation. However, the electrodes show good short-term (14 hour) stability when sulfite hole scavenger is present in the electrolyte, and indefinite stability in both electrolytes in the dark at near-neutral pH. By improving the hole transport efficiency and coating these nanoporous BVO films with an appropriate protective layer and oxygen evolution catalyst, it should be possible to achieve highly efficient and stable water oxidation at a practical pH.

Experimental

Preparation of Mo-free and untextured BVO (noMo/U) films

All synthesis procedures were carried out in air. 0.600 mmol (0.291 g) of $Bi(NO_3)_3{\cdot}5H_2O$ (Sigma Aldrich, >98%) was added to 2.000 g (1.802 mL) of ethylene glycol (Sigma Aldrich, >99%) and sonicated for 5 minutes to obtain a clear and colorless solution. 1.00 mL of glacial acetic acid (Fisher Scientific, >99.7%), 0.50 mL of deionized water, and 0.600 mmol (0.159 g) of $VO(acac)_2$ (Acros Organics, >99%) were added sequentially to this solution and the mixture sonicated for another 20 minutes. To this solution, 236 mg of the triblock copolymer Pluronic F-108 (average M_n ~ 14 600, 82.5 wt% PEG, Aldrich) was added in powder form to serve as a structure directing agent for making highly porous BVO films. Samples made without the polymer were nonporous, large-grain polycrystalline thin films. The solution was sonicated for an additional 30 minutes to obtain a dark green, viscous ink for spin coating. Films were deposited onto FTO-coated glass substrates (TEC 8, Pilkington) at 1200 rpm for 10 seconds followed by 1500 rpm for 40 seconds, then baked on a hotplate at 125 °C for 6 minutes and annealed in a box furnace at 475 °C for 15 minutes using a 10 °C min^{-1} heating rate and a natural cool down to room temperature. This procedure made ~220 nm thick films in a single spin coating step.

Preparation of Mo-containing and untextured BVO (Mo/U) films

To incorporate Mo into the BVO films, an appropriate volume of a 50 mM solution of $MoO_2(acac)_2$ (Sigma Aldrich) in ethylene glycol was added to enough neat ethylene glycol to make a 2.000 g solution. $Bi(NO_3)_3{\cdot}5H_2O$ was then dissolved in this solution and all subsequent processing carried out identically to the noMo/U films described above. Mo at% was determined with respect to Bi. Preparation of 1%, 2%, or 3% Mo spin coating inks required 120 μL, 240 μL, or 360 μL of the $MoO_2(acac)_2$ solution, respectively.

Preparation of textured BVO (noMo/T and Mo/T) films

Films with out-of-plane texture along the [001] direction of BVO were prepared by doubling the mass of $VO(acac)_2$ used for the noMo/U films, increasing the amount of Pluronic F-108 to 350 mg to maintain a constant molar ratio of (V + Bi)/F-108, adjusting the solvent amounts to 1.500 g of ethylene glycol, 2.00 mL acetic acid, and 0.50 mL water, and depositing the films at 700 rpm for 20 seconds followed by 1200 rpm for 40 seconds. To make Mo/T films, Mo was added again with respect to Bi rather than V because the excess V resulted in the formation of V_xO_y phase impurities after annealing. V_xO_y impurities were removed by etching the films in 0.5 M aqueous KOH for 10 seconds, then rinsing with deionized water and drying under a stream of nitrogen. Mo/T films of other thicknesses were produced by adjusting only the solvent amounts and spin coating speed, as follows: 470 nm: 0.500 g EG, 1.50 mL AcOH, 0.30 mL H_2O, 600 rpm for 30 s, then 1200 rpm for 10 s; 370 nm: 1.000 g EG, 1.50 mL AcOH, 0.30 mL H_2O, 600 rpm for 30 s, then 1200 rpm for 10 s; 270 nm: 1.000 g EG, 2.00 mL AcOH, 0.50 mL H_2O, 600 rpm for 30 s, then 1200 rpm for 10 s; 120 nm: 1.500 g EG, 2.00 mL AcOH, 0.50 mL H_2O, 1800 for 10 s, then 2200 rpm for 40 s; 70 nm: 1.500 g EG, 2.00 mL AcOH, 0.50 mL H_2O, 2000 for 5 s, then 2500 rpm for 40 s. All films were made in one spin coating step to avoid layering effects.

Physical characterization

X-ray diffraction data were obtained on a Rigaku SmartLab diffractometer (Cu Kα radiation) at room temperature. Grazing incidence XRD measurements used an angle of incidence of 0.2 degrees. Crystallite size analysis of $\theta/2\theta$ patterns used the Scherrer formula, $\tau = 0.94\lambda \Big/ \sqrt{\left(B_{sample}{}^2 - B_{standard}{}^2\right)} \cos\theta$, where τ is a crystallite thickness, λ the X-ray wavelength, θ the scattering half-angle, B_{sample} the FWHM of the peak in the

Published on 11 February 2016. Downloaded by University of California - Irvine on 11/02/2016 18:07:40.

sample pattern, and $B_{standard}$ the FWHM of the NIST LaB_6 Standard Reference Material 660b under the same experimental conditions. We assumed zero strain broadening and used Voigt line shapes to fit the data. Williamson–Hall and Halder–Wagner plots of the XRD data were too scattered to allow deconvolution of size and strain broadening, probably because the BVO crystallites are anisotropic in shape. Based on the positions of the XRD peaks and the synthesis method used to make the films, the crystallites are expected to have very little strain, so, while the Scherrer values are lower bounds of the average crystallite size, the error from neglecting strain broadening should be small. BVO {004} pole figures were measured using the SmartLab in-plane system with a 2theta-chi goniometer axis and analyzed using the 3D Explore software package. Scanning electron microscopy (SEM) and energy dispersive spectroscopy (EDS) were performed on an FEI Magellan 400L SEM equipped with an Oxford Instruments X-MAX 80 mm^2 detector and AZtecEnergy software. EDS quantification used Tru-Q and the XPP matrix correction algorithm. EDS energy calibration was performed with a NIST copper standard. Raman spectra were obtained using an Renishaw inVia Raman microscope with $\lambda_{incident}$ = 532 nm.

Optical characterization

Room-temperature optical measurements to determine the band gap and absorptance of films on FTO-coated glass substrates were performed on a PerkinElmer Lambda 950 spectrophotometer equipped with a 60 mm integrating sphere. To mimic the EQE measurement conditions as closely as possible, samples were covered with a drop of electrolyte and a quartz coverslip prior to determining their absorptance in the integrating sphere.

Spectroelectrochemical measurements

Spectroelectrochemistry of noMo/U electrodes was conducted using a PerkinElmer Lambda 950 spectrophotometer in 0.2 M KCl buffered to acidic (pH = 2.9), neutral (pH = 6.8), and basic (pH = 9.9) conditions. Measurements were conducted in a direct transmission mode and losses due to reflection at the interface of the working electrode were neglected. A Ag/AgCl (3 M NaCl) reference electrode and a platinum wire counter electrode were used. For potentiostatic measurements, a fixed DC bias was applied for 200 s to achieve steady state prior to recoding the extinction spectrum. For linear sweep potentiodynamic measurements, voltage was swept cathodically (from depletion to accumulation conditions) and the change in extinction at 440 nm monitored (since the bleach due to the Burstein–Moss shift was largest at this wavelength). The intercept of a linear extrapolation of the data with the potential (V) axis was taken as the flatband potential at each pH.

Photoelectrochemical measurements

Three-electrode measurements were performed inside a nitrogen-filled glovebox using a four-neck electrochemical cell fitted with a quartz window. Working electrodes were prepared from films by affixing a long wire to a bare region of the FTO substrate using silver paint (Ted Pella Leitsilber 200), threading the wire through a hollow glass tube, and mounting the sample to the end of the tube using Loctite 9462 Hysol Epoxy. The epoxy encased the entire substrate except for a square-shaped active area of 1.2–1.4 cm^2 exposed to the solution. Biased three-electrode measurements used a saturated calomel electrode (SCE, 4 M KCl) as a reference electrode and a platinum flag as a counter electrode. The electrolyte used for sulfite oxidation was 0.1 M Na_2SO_3 and 0.5 M KH_2PO_4 aqueous phosphate buffer (pH 7.0). We found the current density to be independent of sulfite concentrations above 0.1 M (Fig. S25, ESI†). *J–V* tests showed sulfite to be an efficient hole scavenger for BVO, while other common hole scavengers suffer from either larger dark currents in the scanned potential window (H_2O_2) or inefficient hole transfer (methanol; Fig. S5, ESI†). The electrolyte used for water oxidation was 1.0 M KH_2PO_4 buffer (pH 7.0). *J–V* measurements were obtained by biasing the photoanode using an EG&G PARSTAT 273A potentiostat controlled by the Power Suite package. A Newport 91160A Class A solar simulator fitted with a 300 W xenon arc lamp and an AM1.5G filter was used as the light source. A power density of 100 mW cm^{-2} (1 Sun) was obtained by adjusting the power output of the solar simulator to ~275 W to match the short-circuit current obtained from a NIST-calibrated silicon photodiode (FDSCAL1010, Thorlabs). The power density was confirmed with a pyroelectric radiometer (RkP-575 pyroelectric power probe and Rk-5710 power meter, Laser Probe, Inc.) placed at the sample position. The absolute spectral irradiance of the solar simulator was measured using a USB4000 spectrometer (fiber coupled, with CC-3 cosine corrector) calibrated with a HL-2000-CAL calibrated light source (Ocean Optics). Prior to illuminated measurements, electrodes were cycled in the dark ten times to ensure that stable behavior was achieved. All data were acquired at a scan rate of 10 mV s^{-1}, as faster scan rates resulted in exaggerated currents (Fig. S26, ESI†). Samples were measured both with the light incident from the electrolyte side (EE illumination) and the substrate side (SE illumination) of the film. *J–V* plots as a function of light intensity were acquired using combinations of neutral density filters (Thorlabs). Long-term stability measurements utilized a Schott KG-3 heat-absorbing glass filter to avoid heating of the electrolyte by the infrared output of the solar simulator. The temperature of the electrolyte was monitored with a thermocouple.

Quantum efficiency measurements

External quantum efficiency (EQE) measurements for both sulfite and water oxidation were performed using the three-electrode setup described above. An Oriel Cornerstone 260 0.25 m monochromator equipped with a 150 W xenon arc lamp served as the light source. The exit slit of the monochromator was adjusted to obtain a bandwidth of 10 nm. Photocurrent was measured with a Keithley 2400 Source Measure Unit controlled by LabView software. The working electrode was held at a fixed potential against the SCE reference and the current between it and the counter electrode (platinum flag) was monitored. All photocurrent spectra were obtained using chopped illumination (10 seconds dark and 10 seconds light for each wavelength) with the last 8 seconds of each cycle averaged to obtain the net photocurrent at each wavelength. A silicon photodiode

 This journal is © The Royal Society of Chemistry 2016

Published on 11 February 2016. Downloaded by University of California - Irvine on 11/02/2016 18:07:40.

(SMP1D1A, Thorlabs) calibrated by Newport Corp. was used as the reference. The EQE was calculated using the equation:

$$\mathrm{EQE}(\lambda) = (I_{\mathrm{BVO}}/I_{\mathrm{Si}}) \times \mathrm{EQE}_{\mathrm{Si}}(\lambda).$$

The IQE of each device was obtained as

$$\mathrm{IQE}(\lambda) = \mathrm{EQE}(\lambda)/\mathrm{absorptance}(\lambda)$$

where the absorptance is that of the BVO layer.

Optical modeling

Optical modeling of BVO electrodes was carried out using a 1D transfer-matrix model[62] implemented in Igor Pro 6.36. Model inputs are the layer sequence of the electrode and the optical constants (n and k) and thicknesses of each layer (*i.e.*, BVO, FTO, adhesion layer, SnO_2, glass). The model calculates total transmittance, reflectance, absorptance, and the absorptance of each layer of the electrode at each wavelength as well as the electric field and photon absorption rate *versus* wavelength and position for a specified illuminating spectrum (*e.g.*, AM1.5G). Optical constants for BVO and TEC 8 glass were taken from ref. 7 and 86, respectively. Optical constants for the porous, electrolyte filled BVO films and the mixed BVO/FTO interlayer were calculated with the Bruggeman effective medium approximation.

Ultraviolet photoemission and X-ray photoemission spectroscopy

XPS and UPS experiments at NREL were performed using a modified PHI 5600 photoemission system that has been described previously.[87] Films were measured both with and without cleaning by deionized water rinse and *ex situ* UV-ozone exposure to reduce sodium and carbon contamination. High resolution XPS data were acquired at normal take-off angle using a pass energy of 11.75 eV. The binding energy scale of the instrument was calibrated using photoelectron lines at low and high energy from sputter-cleaned gold and copper. The Fermi energy calibration used sputter-cleaned Mo foil. Satellites in UPS spectra were numerically subtracted from spectra acquired under a bias of −45 V. Atomic compositions were calculated using literature sensitivity factors and the PHI MultiPak 9.5.1.0 software package. *In situ* atomic hydrogen exposures were performed at a chamber pressure of 10^{-7} Torr using an Oxford Applied Research TC-50 thermal cracker operating at 45 W.

Photoemission data were also acquired at UCI using a Kratos AXIS Supra spectrometer (monochromated Al source, normal take-off angle). Survey and high-resolution core-level spectra were collected at 160 eV and 20 eV pass energies, respectively. Binding energy scale calibration was performed using a sputter-cleaned Ag foil. High-resolution X-ray and ultraviolet excited valence band spectra were collected at 10 eV pass energy. UPS data were collected using the He(I) line (40 mA emission current). Fermi edge calibration was performed with a sputter-cleaned Ag foil. Ion scattering spectroscopy was performed on the Supra spectrometer using 1 keV He^+ ions in a 135° fixed-angle scattering geometry. Scattered ions were collected with energies of 100–1000 eV at a 160 eV pass energy using a 1 eV step size, 300 ms dwell time, and 5 sweeps per spectrum.

Conflict of interest disclosure

The authors declare no competing financial interest.

Acknowledgements

V. N. and M. L. thank the UC Solar Institute (UC Multicampus Research Programs and Initiatives grant MR-15-328386), the Alfred P. Sloan Foundation, and the UC Irvine Center for Solar Energy for funding. C. L. P. acknowledges support by the U.S. Department of Energy under Contract No. DE-AC36-08-GO28308 with the National Renewable Energy Laboratory. SEM and XRD studies were performed at the Laboratory for Electron and X-ray Instrumentation (LEXI) and Raman studies at the Laser Spectroscopy Facility (LSF) at UC Irvine. XPS and ISS studies at UC Irvine utilized equipment funded in part by the Major Research Instrumentation program of the National Science Foundation under Grant No. CHE-1338173.

References

1 A. Kudo, K. Ueda, H. Kato and I. Mikami, Photocatalytic O_2 evolution under visible light irradiation on $BiVO_4$ in aqueous $AgNO_3$ solution, *Catal. Lett.*, 1998, **53**, 229–230.
2 Y. Park, K. J. McDonald and K.-S. Choi, Progress in bismuth vanadate photoanodes for use in solar water oxidation, *Chem. Soc. Rev.*, 2013, **42**, 2321–2337.
3 K. Sivula, Metal oxide photoelectrodes for solar fuel production, surface traps, and catalysis, *J. Phys. Chem. Lett.*, 2013, **4**, 1624–1633.
4 Z.-F. Huang, L. Pan, J.-J. Zou, X. Zhang and L. Wang, Nanostructured bismuth vanadate-based materials for solar-energy-driven water oxidation: a review on recent progress, *Nanoscale*, 2014, **6**, 14044–14063.
5 J. H. Kim and J. S. Lee, $BiVO_4$-based heterostructured photocatalysts for solar water splitting: a review, *Energy Environ. Focus*, 2014, **3**, 339–353.
6 J. K. Cooper, S. Gul, F. M. Toma, L. Chen, Y.-S. Liu, J. Guo, J. W. Ager, J. Yano and I. D. Sharp, Indirect bandgap and optical properties of monoclinic bismuth vanadate, *J. Phys. Chem. C*, 2015, **119**, 2969–2974.
7 Z. Zhao, Z. Li and Z. Zou, Electronic structure and optical properties of monoclinic clinobisvanite $BiVO_4$, *Phys. Chem. Chem. Phys.*, 2011, **13**, 4746–4753.
8 J. A. Seabold and K. S. Choi, Efficient and stable photo-oxidation of water by a bismuth vanadate photoanode couples with an iron oxyhydroxide oxygen evolution catalyst, *J. Am. Chem. Soc.*, 2012, **134**, 2186–2192.
9 T. W. Kim and K.-S. Choi, Nanoporous $BiVO_4$ photoanodes with dual-layer oxygen evolution catalysts for solar water splitting, *Science*, 2014, **343**, 990–994.
10 T. W. Kim, Y. Ping, G. A. Galli and K.-S. Choi, Simultaneous enhancements in photon absorption and charge transport in bismuth vanadate photoanodes for solar water splitting, *Nat. Commun.*, 2015, **6**, 8769.

Published on 11 February 2016. Downloaded by University of California - Irvine on 11/02/2016 18:07:40.

11 A. Walsh, Y. Yan, M. N. Huda, M. M. Al-Jassim and S. H. Wei, Band edge electronic structure of $BiVO_4$: Elucidating the role of the Bi s and V d orbitals, *Chem. Mater.*, 2009, **21**, 547–551.
12 J. K Cooper, S. Gul, F. M. Toma, L. Chen, P.-A. Glans, J. Guo, J. W. Ager, J. Yano and I. D. Sharp, Electronic structure of monoclinic $BiVO_4$, *Chem. Mater.*, 2014, **26**, 5365–5373.
13 C. Jiang, R. Wang and B. A. Parkinson, Combinatorial approach to improve photoelectrodes based on $BiVO_4$, *ACS Comb. Sci.*, 2013, **15**, 639–645.
14 D. K. Zhong, S. Choi and D. R. Gamelin, Near-complete suppression of surface recombination in solar photoelectrolysis by Co-Pi catalyst-modified W:$BiVO_4$, *J. Am. Chem. Soc.*, 2011, **133**, 18370–18377.
15 F. F. Abdi, T. J. Savenije, M. M. May, B. Dam and R. van de Krol, The origin of slow carrier transport in $BiVO_4$ thin film photoanodes: A time-resolved microwave conductivity study, *J. Phys. Chem. Lett.*, 2013, **4**, 2752–2757.
16 R. A. Pala, A. L. Leenheer, M. Lichterman, H. A. Atwater and N. S. Lewis, Measurement of minority-carrier diffusion lengths using wedge-shaped semiconductor photoelectrodes, *Energy Environ. Sci.*, 2014, **7**, 3424–3430.
17 A. J. E. Rettie, H. C. Lee, L. G. Marshall, J.-F. Lin, C. Capan, J. Lindemuth, J. S. McCloy, J. Zhou, A. J. Bard and C. B. Mullins, Combined charge carrier transport and photoelectrochemical characterization of $BiVO_4$ single crystals: intrinsic behavior of a complex metal oxide, *J. Am. Chem. Soc.*, 2013, **135**, 11389–11396.
18 J. A. Seabold, K. Zhu and N. R. Neale, Efficient solar photoelectrolysis by nanoporous Mo:$BiVO_4$ through controlled electron transport, *Phys. Chem. Chem. Phys.*, 2014, **16**, 1121–1131.
19 L. Chen, E. A. Lladó, M. Hettick, I. D. Sharp, Y. Lin, A. Javey and J. W. Ager, Reactive sputtering of bismuth vanadate photoanodes for solar water splitting, *J. Phys. Chem. C*, 2013, **117**, 21635–21642.
20 F. F. Abdi and R. van der Krol, Nature and light dependence of bulk recombination in Co-Pi-catalyzed $BiVO_4$ photoanodes, *J. Phys. Chem. C*, 2012, **116**, 9398–9404.
21 S. K. Pilli, T. E. Furtak, L. D. Brown, T. G. Deutsch, J. A. Turner and A. M. Herring, Cobalt-phosphate (Co-Pi) catalyst modified Mo-doped $BiVO_4$ photoelectrodes for solar water oxidation, *Energy Environ. Sci.*, 2011, **4**, 5028–5034.
22 M. T. McDowell, M. F. Lichterman, J. M. Spurgeon, S. Hu, I. D. Sharp, B. S. Brunschwig and N. S. Lewis, Improved stability of polycrystalline bismuth vanadate photoanodes by use of dual-layer thin TiO_2/Ni coatings, *J. Phys. Chem. C*, 2014, **118**, 19618–19624.
23 J. Jin, K. Walczak, M. R. Singh, C. Karp, N. S. Lewis and C. Xiang, An experimental and modeling/simulation-based evaluation of the efficiency and operational performance characteristics of an integrated, membrane-free, neutral pH solar-driven water-splitting system, *Energy Environ. Sci.*, 2014, **7**, 3371–3380.
24 W. Luo, Z. Li, T. Yu and Z. Zou, Effects of surface electrochemical pretreatment on the photoelectrochemical performance of Mo-doped $BiVO_4$, *J. Phys. Chem. C*, 2012, **116**, 5076–5081.
25 S. K. Pilli, R. Janarthanan, T. G. Deutsch, T. E. Furtak, L. D. Brown, J. A. Turner and A. M. Herring, Efficient photoelectrochemical water oxidation over cobalt phosphate catalyst modified $BiVO_4$/1D-WO_3 heterojunction electrodes, *Phys. Chem. Chem. Phys.*, 2013, **15**, 14723–14728.
26 W. Yao, H. Iwai and J. Ye, Effects of molybdenum substitution on the photocatalytic behavior of $BiVO_4$, *Dalton Trans.*, 2008, 1426–1430.
27 Z. Zhao, W. Luo, Z. Li and Z. Zou, Density functional theory study of doping effects in monoclinic clinobisvanite $BiVO_4$, *Phys. Lett. A*, 2010, **374**, 4919–4927.
28 H. Ye, J. Lee, J. S. Jang and A. J. Bard, Rapid screening of $BiVO_4$-based photocatalyst by scanning electrochemical microscopy (SECM) and studies of their photoelectrochemical properties, *J. Phys. Chem. C*, 2010, **114**, 13322–13328.
29 M. Li, L. Zhao and L. Guo, Preparation and photoelectrochemical study of $BiVO_4$ thin films deposited by ultrasonic spray pyrolysis, *Int. J. Hydrogen Energy*, 2010, **35**, 7127–7133.
30 W. Luo, Z. Yang, Z. Li, J. Zhang, J. Liu, Z. Zhao, Z. Wang, S. Yan, T. Yu and Z. Zou, Solar hydrogen generation from seawater with a modified $BiVO_4$ photoanode, *Energy Environ. Sci.*, 2011, **4**, 4046–4051.
31 H. S. Park, K. E. Kweon, H. Ye, E. Paek, G. S. Hwang and A. J. Bard, Factors in the metal doping of $BiVO_4$ for improved photoelectrochemical activity as studied by scanning electrochemical microscopy and first-principles density-functional theory, *J. Phys. Chem. C*, 2011, **115**, 17870–17879.
32 Y. Liang, T. Tsubota, L. P. A. Mooij and R. van de Krol, Highly improved quantum efficiencies for thin film $BiVO_4$ photoanodes, *J. Phys. Chem. C*, 2011, **115**, 17594–17598.
33 W.-J. Yin, S.-H. Wei, M. M. Al-Jassim, J. Turner and Y. Yan, Doping properties of monoclinic $BiVO_4$ studied by first-principles density-functional theory, *Phys. Rev. B: Condens. Matter Mater. Phys.*, 2011, **83**, 155102.
34 S. P. Berglund, A. J. E. Rettie, S. Hoang and C. B. Mullins, Incorporation of Mo and W into nanostructured $BiVO_4$ films for efficient photoelectrochemical water oxidation, *Phys. Chem. Chem. Phys.*, 2012, **14**, 7065–7075.
35 K. Zhang, X.-J. Shi, J. K. Kim and J. H. Park, Photoelectrochemical cells with tungsten trioxide/Mo-doped $BiVO_4$ bilayers, *Phys. Chem. Chem. Phys.*, 2012, **14**, 11119–11124.
36 Y. Hou, F. Zuo, A. Dagg and P. Feng, Visible light-driven α-Fe_2O_3 nanorod/graphene/$BiV_{1-x}Mo_xO_4$ core/shell heterojunction array for efficient photoelectrochemical water splitting, *Nano Lett.*, 2012, **12**, 6464–6473.
37 H. W. Jeong, T. H. Jeon, J. S. Jang, W. Choi and H. Park, Strategic modification pf $BiVO_4$ for improving photoelectrochemical water oxidation performance, *J. Phys. Chem. C*, 2013, **117**, 9104–9112.
38 G. Wang, Y. Ling, X. Lu, F. Qian, Y. Tong, J. Z. Zhang, V. Lordi, C. R. Leao and Y. Li, Computational and photoelectrochemical study of hydrogenated bismuth vanadate, *J. Phys. Chem. C*, 2013, **117**, 10957–10964.
39 F. F. Abdi, L. Han, A. H. M. Smets, M. Zeman, B. Dam and R. van de Krol, Efficient solar water splitting by enhanced

 This journal is © The Royal Society of Chemistry 2016

Published on 11 February 2016. Downloaded by University of California - Irvine on 11/02/2016 18:07:40.

charge separation in bismuth vanadate-silicon tandem photoelectrode, *Nat. Commun.*, 2013, **4**, 2195.

40 W. Luo, J. Wang, X. Zhao, Z. Zhao, Z. Li and Z. Zou, Formation energy and photoelectrochemical properties of $BiVO_4$ after doping at Bi^{3+} and V^{5+} sites with higher valence metal ions, *Phys. Chem. Chem. Phys.*, 2013, **15**, 1006–1013.

41 S. K. Cho, H. S. Park, H. C. Lee, K. M. Nam and A. J. Bard, Metal doping of $BiVO_4$ by composite electrodeposition with improved photoelectrochemical water oxidation, *J. Phys. Chem. C*, 2013, **117**, 23048–23056.

42 Y. Park, D. Kang and K.-S. Choi, Marked enhancement in electron-hole separation achieved in the low bias region using electrochemically prepared Mo-doped $BiVO_4$ photoanodes, *Phys. Chem. Chem. Phys.*, 2014, **16**, 1238–1246.

43 L. Han, F. F. Abdi, P. P. Rodriguez, B. Dum, R. van de Krol, M. Zeman and A. H. M. Smets, Optimization of amorphous silicon double junction solar cells for an efficient photoelectrochemical water splitting device based on a bismuth vanadate photoanode, *Phys. Chem. Chem. Phys.*, 2014, **16**, 4220–4229.

44 P. Chatchai, Y. Murakami, S.-y. Kishioka, A. Y. Nosaka and Y. Nosaka, FTO/SnO_2/$BiVO_4$ composite photoelectrode for water oxidation under visible light irradiation, *Electrochem. Solid-State Lett.*, 2008, **11**, H160–H163.

45 M. Long, W. Cai and H. Kisch, Visible light induced photoelectrochemical properties of n-$BiVO_4$/p-Co_3O_4, *J. Phys. Chem. C*, 2008, **112**, 548–554.

46 J. Su, X.-X. Zou, G.-D. Li, X. Wei, C. Yan, Y.-N. Wang, J. Zhao, L.-J. Zhou and J.-S. Chen, Macroporous V_2O_5-$BiVO_4$ composites: effect of heterojunction on the behavior of photogenerated charges, *J. Phys. Chem. C*, 2011, **115**, 8064–8071.

47 J. Su, L. Guo, N. Bao and C. A. Grimes, Nanostructured WO_3/$BiVO_4$ heterojunction films for efficient photoelectrochemical water splitting, *Nano Lett.*, 2011, **11**, 1928–1933.

48 F. F. Abdi, N. Firet and R. van de Krol, Efficient $BiVO_4$ thin film photoanodes modified with cobalt phosphate catalyst and W-doping, *ChemCatChem*, 2013, **5**, 490–496.

49 P. M. Rao, L. Cai, C. Liu, I. S. Cho, C. H. Lee, J. M. Weisse, P. Yang and X. Zheng, Simultaneously efficient light absorption and charge separation in WO_3/$BiVO_4$ core/shell nanowire photoanode for photoelectrochemical water oxidation, *Nano Lett.*, 2014, **14**, 1099–1105.

50 M. Zhong, T. Hisatomi, Y. Kuang, J. Zhao, M. Liu, A. Iwase, Q. Jia, H. Nishiyama, T. Minegishi, M. Nakabayshi, N. Shibata, R. Niishiro, C. Katayama, H. Shibano, M. Katayama, A. Kudo, T. Yamada and K. Domen, Surface modification of CoO_x loaded $BiVO_4$ photoanodes with ultrathin *p*-type NiO layers for improved solar water oxidation, *J. Am. Chem. Soc.*, 2015, **137**, 5053–5060.

51 K. Sayama, A. Nomura, T. Arai, T. Sugita, R. Abe, M. Yanagida, T. Oi, Y. Iwasaki, Y. Abe and H. Sugihara, Photoelectrochemical decomposition of water into H_2 and O_2 on porous $BiVO_4$ thin-film electrodes under visible light and significant effect on Ag ion treatment, *J. Phys. Chem. B*, 2006, **110**, 11352–11360.

52 T. H. Jeon, W. Choi and H. Park, Cobalt-phosphate complexes catalyze the photoelectrochemical water oxidation of $BiVO_4$ electrodes, *Phys. Chem. Chem. Phys.*, 2011, **13**, 21392–21401.

53 D. Wang, R. Li, J. Zhu, J. Shi, J. Han, X. Zong and C. Li, Photocatalytic water oxidation on $BiVO_4$ with the electrocatalyst as an oxidation cocatalyst: Essential relations between electrocatalyst and photocatalyst, *J. Phys. Chem. C*, 2012, **116**, 5082–5089.

54 M. F. Lichterman, M. R. Shaner, S. G. Handler, B. S. Brunschwig, H. B. Gray, N. S. Lewis and J. M. Spurgeon, Enhanced stability and activity for water oxidation in alkaline media with bismuth vanadate photoelectrodes modified with cobalt oxide catalytic layer produced by atomic layer deposition, *J. Phys. Chem. Lett.*, 2013, **4**, 4188–4191.

55 C. Ding, J. Shi, D. Wang, Z. Wang, N. Wang, G. Liu, F. Xiong and C. Li, Visible light driven overall water splitting using cocatalyst/$BiVO_4$ photoanode with minimized bias, *Phys. Chem. Chem. Phys.*, 2013, **15**, 4589–4595.

56 P. Bornoz, F. F. Abdi, S. D. Tiley, B. Dam, R. van de Krol, M. Graetzel and K. Sivula, A bismuth vanadate-cuprous oxide tandem cell for overall solar water splitting, *J. Phys. Chem. C*, 2014, **118**, 16959–16966.

57 R. L. Frost, D. A. Henry, M. L. Weier and W. Martens, Raman spectroscopy of three polymorphs of $BiVO_4$: clinobisvanite, dreyerite and pucherite, with comparisons to $(VO_4)^{3-}$-bearing minerals: namibite, pottsite and schumacherite, *J. Raman Spectrosc.*, 2006, **37**, 722–732.

58 A. J. Bard, R. Parsons and J. Jordan, *Standard Potentials in Aqueous Solution*, Marcel Dekker, Inc., New York, 1985.

59 W. P. Gomes, T. Freund and S. R. Morrison, Chemical reactions involving holes at the zinc oxide single crystal anode, *J. Electrochem. Soc.*, 1968, **115**, 818–823.

60 B. O'Regan, M. Graetzel and D. Fitzmaurice, Optical electrochemistry I: steady-state spectroscopy of conduction-band electrons in a metal oxide semiconductor electrode, *Chem. Phys. Lett.*, 1991, **183**, 89–93.

61 N. Kopidakis, E. A. Schiff, N.-G. Park, J. van de Lagemaat and A. J. Frank, Ambipolar diffusion of photocarriers in electrolyte-filled, nanoporous TiO_2, *J. Phys. Chem. B*, 2000, **104**, 3930–3936.

62 M. Law, M. C. Beard, S. Choi, J. M. Luther, M. C. Hanna and A. J. Nozik, Determining the internal quantum efficiency of PbSe nanocrystal solar cells with the aid of an optical model, *Nano Lett.*, 2008, **8**, 3904–3910.

63 S. Tokunaga, H. Kato and A. Kudo, Selective preparation of monoclinic and tetragonal $BiVO_4$ with scheelite structure and their photocatalytic properties, *Chem. Mater.*, 2001, **13**, 4624–4628.

64 M. Cesari, G. Perrego, A. Zazzetta, G. Manara and B. Notari, The crystal structures of the bismuth molybdovanadates and of the α-phase bismuth molybdate, *J. Inorg. Nucl. Chem.*, 1971, **33**, 3595–3597.

65 A. W. Sleight, K. Aykan and D. B. Rogers, New nonstoichiometric molybdate, tungstate, and vanadate catalysts with the Scheelite-type structure, *J. Solid State Chem.*, 1975, **13**, 213–236.

66 W. Yao and J. Ye, Photophysical and photocatalytic properties of $Ca_{1-x}Bi_xV_xMo_{1-x}O_4$ solid solutions, *J. Phys. Chem. B*, 2006, **110**, 11188–11195.

Published on 11 February 2016. Downloaded by University of California - Irvine on 11/02/2016 18:07:40.

67 W. Guo, T. L. Ward, C. Porter and A. K. Datye, Phase content and particle morphology of Bi-Mo-V-O powders produced by aerosol pyrolysis, *Mater. Res. Bull.*, 2005, **40**, 1371–1387.
68 T. Duraisamy and A. Ramanan, $Na_{x/2}Bi_{1-x/2}Mo_xV_{1-x}O_4$ and $Bi_{1-x/3}Mo_xV_{1-x}O_4$: New Scheelite-related phases, *Solid State Ionics*, 1999, **120**, 233–237.
69 I. Cesar, K. Sivula, A. Kay, R. Zboril and M. Grätzel, Influence of feature size, film thickness, and silicon doping on the performance of nanostructured hematite photoanodes for solar water splitting, *J. Phys. Chem. C*, 2009, **113**, 772–782.
70 Y.-S. Hu, A. Kleiman-Shwarsctien, A. J. Forman, D. Hazen, J.-N. Park and E. W. McFarland, Pt-doped α-Fe_2O_3 thin films for photoelectrochemical water splitting, *Chem. Mater.*, 2008, **20**, 3803–3805.
71 L. Hoffart, U. Heider, R. A. Huggins, W. Witschel, R. Jooss and A. Lentz, Crystal growth and conductivity investigations on $BiVO_4$ single crystals, *Ionics*, 1996, **2**, 34–38.
72 W. Hayes and R. Loudon, *Scattering of light by crystals*, Wiley, New York, 1978.
73 K. Mizoguchi and S. Nakashima, Determination of crystallographic orientations in silicon films by Raman-microprobe polarization measurements, *J. Appl. Phys.*, 1989, **65**, 2583–2590.
74 Y. Schuhl Y, H. Baussart, R. Delobel, M. Le Bras, J. Leroy, L. G. Gengembre and J. J. Rimblot, Study of mixed-oxide catalysts containing bismuth, vanadium and antimony. Preparation, phase composition, spectroscopic characterization and catalytic oxidation of propene, *J. Chem. Soc., Faraday Trans. 1*, 1983, **79**, 2055–2069.
75 A. V. Naumkin, A. Kraut-Vass, S. W. Gaarenstroom and C. J. Powell, *NIST X-ray Photoelectron Spectroscopy Database 20, Version 4.1*, National Institute of Standards and Technology, Gaithersburg, 2012http://srdata.nist.gov/xps/.
76 G. Silversmit, D. Depla, H. Poelman, G. B. Marin and R. De Gryse, Determination of the V2p XPS binding energies for difference vanadium oxidation states (V^{5+} to V^{0+}), *J. Electron Spectrosc. Relat. Phenom.*, 2004, **135**, 167–175.
77 M. D. Rossell, P. Agrawal, A. Borgschulte, C. Hébert, D. Passerone and R. Erni, Direct evidence of surface reduction in monoclinic $BiVO_4$, *Chem. Mater.*, 2015, **27**, 3593–3600.
78 T. S. Sinclair, B. M. Hunter, J. R. Winkler, H. B. Gray and A. M. Müller, Factors affecting bismuth vanadate photoelectrochemical performance, *Mater. Horiz.*, 2015, **2**, 330–337.
79 J.-L. Pouchou, X-Ray microanalysis of stratified specimens, *Anal. Chim. Acta*, 1983, **283**, 81–97.
80 J.-L. Pouchou and F. Pichoir, *Microbeam Analysis*, San Francisco Press, 1988, p.249.
81 H. Niehus, W. Heiland and E. Taglauer, Low-energy ion scattering at surfaces, *Surf. Sci. Rep.*, 1993, **17**, 213–303.
82 A. P. Singh, N. Kodan, A. Dey, S. Krishnamurthy and B. R. Mehta, Improvement in the structural, optical, electronic and photoelectrochemical properties of hydrogen treated bismuth vanadate thin films, *Int. J. Hydrogen Energy*, 2015, **40**, 4311–4319.
83 D.-D. Qin, T. Wang, Y.-M. Song and C.-L. Tao, Reduced monoclinic $BiVO_4$ for improved photoelectrochemical oxidation of water under visible light, *Dalton Trans.*, 2014, **43**, 7691–7694.
84 R. Li, F. Zhang, D. Wang, J. Yang, M. Li, J. Zhu, X. Zhou, H. Han and C. Li, Spatial separation of photogenerated electrons and holes among {010} and {110} crystal facets of $BiVO_4$, *Nat. Commun.*, 2012, **4**, 1432.
85 R. Munprom, P. A. Salvador and G. S. Rohrer, The orientation dependence of the photochemical reactivity of $BiVO_4$, *J. Mater. Chem. A*, 2015, **3**, 2370–2377.
86 J. Chen, *Spectroscopic ellipsometry studies of II-VI semiconductor materials and solar cells*, PhD thesis, The University of Toledo, 2010.
87 C. L. Perkins and F. S. Hasoon, Surfactant-assisted growth of CdS thin films for photovoltaic applications, *J. Vac. Sci. Technol., A*, 2006, **24**, 497–504.

 This journal is © The Royal Society of Chemistry 2016